Stabilized Shock Hydrodynamics: V. Von Neumann Stability Analysis of a Predictor/Multi-corrector Lagrangian Method☆

G. Scovazzi[a,*], W. J. Rider[a], E. Love[a], J. N. Shadid[b]

[a] *1431 Computational Shock- and Multi-physics Department, Sandia National Laboratories, P.O. Box 5800, MS 1319, Albuquerque, NM 87185-1319, USA*
[b] *1437 Electrical and Microsystem Modeling Department, Sandia National Laboratories, P.O. Box 5800, MS 0378, Albuquerque, NM 87185-0378, USA*

Abstract

The typical structure of the linearized equations of Lagrangian shock-hydrodynamics is given by the first-order system form of the wave equation with dissipative effects. This article presents the complete von Neumann stability and dispersion analysis for a predictor/multi-corrector time integrator applied to a stabilized variational multiscale finite element formulation of such system of equations. Bounds for stable time advancement are derived, and estimates of the formal order of accuracy indicate that the proposed method is second order in time and space.

Key words: von Neumann stability analysis, predictor/multi-corrector algorithm, mid-point time integrator, Lagrangian shock hydrodynamics, stabilized methods, variational multiscale analysis, hourglass control, pressure instabilities, nodal finite element method.

1. Introduction

In [8, 12], a conservative predictor multi-corrector time integrator was proposed in combination with a new Lagrangian shock hydrodynamics algorithm based on piece-wise linear finite elements and variational multiscale stabilization. This article presents the full von Neumann analysis of stability for this algorithm, in the case of a linearized version of the shock hydrodynamics equations. The linearized system of equations governs the acoustic propagation of waves in a medium.

Because the proposed algorithm is often used in combination with shock capturing artificial viscosities, stability bounds are derived not only in the case of a purely acoustic, undamped system of equations, but also in the case when diffusion is present. As expected, the presence of stiff diffusion-type operators is negatively affecting the stability of the time integration scheme, producing a more restrictive Courant-Friedriechs-Levy condition. A simple time-step control condition is developed by analyzing the stability of the highest wave numbers in the discrete system of equations, and compared with results from the complete von Neumann analysis. Furthermore, by means of Taylor series expansions, it is shown that the formal accuracy of the method in the case of no artificial viscosity is second order in time and space.

☆This research was partially funded by the DOE NNSA Advanced Scientific Computing Program and the Computer Science Research Institute at Sandia National Laboratories. Sandia is a multiprogram laboratory operated by Sandia Corporation, a Lockheed Martin Company, for the United States Department of Energy under contract DEAC04-94-AL85000.

*Corresponding author
Email addresses: gscovaz@sandia.gov (G. Scovazzi)

The rest of the exposition is organized as follows: Section 2 is devoted to presenting the equations of Lagrangian hydrodynamics, deriving an appropriate and representative linearization. In Section 3, the discrete system of equations is obtained in the case of one dimension and periodic boundary conditions. By means of the Discrete Fourier Transform, the von Neumann stability analysis is applied in Section 4 to the full system of discrete modes, and restricted in Section 5 to the highest wave numbers, with the purpose of deriving a simple stability bound for the time step in practical computations. Section 6 is devoted to the analysis of the system of equations of pure (undamped) acoustics, and includes calculations of the formal order of accuracy of the method by Taylor expansion of the dissipation and dispersion errors. In Section 7 the effects of viscosity on stability are also accounted for. A few numerical tests are presented in Section 8, to verify the stability estimates derived in previous sections. Conclusions are summarized in Section 9.

2. A simplified Lagrangian hydrodynamics system

With the purpose of presenting the algorithm proposed in [8, 12], we briefly summarize the system of Lagrangian equations for a compressible fluid in which heat fluxes, heat sources, and body forces are absent. Let Ω_0 and Ω be open sets in $\mathbb{R}^{n_d}$ (where n_d is the number of spatial dimensions). The *deformation*

$$\varphi : \Omega_0 \to \Omega = \varphi(\Omega_0) \,, \tag{1}$$

$$\boldsymbol{X} \mapsto \boldsymbol{x} = \varphi(\boldsymbol{X}, t) \,, \quad \forall \boldsymbol{X} \in \Omega_0, \; t \geq 0 \,, \tag{2}$$

maps the material coordinate $\boldsymbol{X}$, representing the initial position of an infinitesimal material particle of the body, to $\boldsymbol{x}$, the position of that particle in the current configuration (see Fig. 1). Ω_0

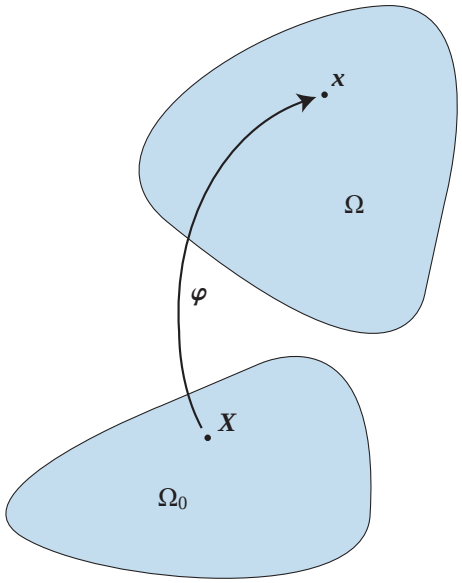

Figure 1: Sketch of the Lagrangian map $\boldsymbol{\varphi}$.

is the domain occupied by the body in its initial configuration, with boundary Γ_0. $\boldsymbol{\varphi}$ maps Ω_0 to Ω, the domain occupied by the body in its current configuration. The *deformation gradient* and *deformation Jacobian determinant* can be defined as

$$\boldsymbol{F} = \nabla_X \boldsymbol{\varphi} \,, \tag{3}$$

$$J = \det(\boldsymbol{F}) \,, \tag{4}$$

where ∇_X is the gradient in the original configuration. In the domain Ω, the equations for the displacement update and conservation of mass, momentum, and energy read:

$$\dot{\boldsymbol{u}} = \boldsymbol{v} \,, \tag{5}$$

$$\rho J = \rho_0 \,, \tag{6}$$

$$0 = \rho \dot{\boldsymbol{v}} + \nabla_x p \,, \tag{7}$$

$$0 = \rho \dot{\epsilon} + p \nabla_x \cdot \boldsymbol{v} \,. \tag{8}$$

Here, ∇_x and $\nabla_x \cdot$ are the current configuration gradient and divergence operators, and $(\dot{\cdot})$ indicates the material, or Lagrangian, time derivative. $\boldsymbol{u} = \boldsymbol{x} - \boldsymbol{X}$ is the displacement vector, ρ_0 is the reference (initial) density, ρ is the (current) density, $\boldsymbol{v}$ is the velocity, and p is the pressure, assumed to satisfy an equation of state of the form $p = \hat{p}(\rho, \epsilon)$, with ϵ the internal energy per unit mass.

In [8], it was shown that the shock hydrodynamics equations can be reduced to the system (or, mixed) form of a nonlinear wave equation. Namely, (6), (7), (8), and the equation of state yield

$$0 = \rho \dot{\boldsymbol{v}} + \nabla_x p \,, \tag{9}$$

$$0 = \dot{p} + \rho c_s^2 \nabla_x \cdot \boldsymbol{v} \,, \tag{10}$$

where c_s is the speed of sound in the medium. In the Lagrangian setting, the displacement and mass conservation equations (5)-(6) are associated with a standing entropy wave (with respect to the Lagrangian material coordinates) governing the motion of contact discontinuities. The incorporation of these equations in the analysis that follows is not essential, as the stability bounds for the system of equations under consideration are dominated by the acoustic characteristics associated with equations (9) and (10). In this context, it is also important to observe that, by construction, numerical schemes in Lagrangian coordinates are capable of precisely capturing and tracking contact discontinuities without adding any numerical dissipation. Therefore, we will restrict our analysis to the system of equations (9) and (10), which can be easily linearized assuming small strains (implying $\nabla_x \approx \nabla_X$, i.e., negligible mesh motion), and small space/time variations of density and speed of sound.

In order to achieve insightful results, we will consider a simple one-dimensional flow with periodic boundary conditions. The reader will appreciate in what follows that the derivations are quite involved, and that these assumptions are essential to obtain meaningful results.

3. One-dimensional linearized variational formulation

Analogous to [12], we consider a weak formulation of the one-dimensional linearized equations of Lagrangian shock hydrodynamics, augmented by variational multiscale stabilization operators and a shock capturing artificial viscosity operator. Namely, denoting by $\mathbb{T}$ the unit periodic torus along the real line $\mathbb{R}$, and considering a piece-wise linear finite element decomposition, we have that, for every discrete test functions ψ and ϕ,

$$\begin{aligned} 0 = & \int_{\mathbb{T}} \psi \, \dot{V} - \int_{\mathbb{T}} \psi_{,X} \, P \\ & + \int_{\mathbb{T}} \psi_{,X} \, \tau (\dot{P} + c_s^2 V_{,X}) + \int_{\mathbb{T}} \psi_{,X} \, \nu_V \, V_{,X} \,, \end{aligned} \tag{11}$$

$$\begin{aligned} 0 = & \int_{\mathbb{T}} \phi \, \dot{P} + \int_{\mathbb{T}} \phi \, c_s^2 \, V_{,X} \\ & + \int_{\mathbb{T}} \phi_{,X} \, \tau c_s^2 (\dot{V} + P_{,X}) + \int_{\mathbb{T}} \phi_{,X} \, \nu_P \, P_{,X} \,, \end{aligned} \tag{12}$$

where we have used the notation $V = \rho v$ (recall $\rho = \text{const.}$) and $P = p$. For the sake of simplicity, we also assume $\nu_V = \nu_P = \nu$. Using the same predictor/multi-corrector strategy adopted in [12], the discretization in time of (11)-(12) yields:

$$\begin{aligned} 0 = & \int_{\mathbb{T}} \psi \left(V_{n+1}^{(i+1)} - V_n \right) - \Delta t \int_{\mathbb{T}} \psi_{,X} \, P_{n+1/2}^{(i)} \\ & + \Delta t \int_{\mathbb{T}} \psi_{,X} \, \tilde{\tau} \left(P_{n+1}^{(i)} - P_n + \Delta t c_s^2 (V_{,X})_{n+1/2}^{(i)} \right) \\ & + \Delta t \int_{\mathbb{T}} \psi_{,X} \, \nu \, (V_{,X})_{n+1/2}^{(i)} \,, \end{aligned} \tag{13}$$

$$\begin{aligned} 0 = & \int_{\mathbb{T}} \phi \left(P_{n+1}^{(i+1)} - P_n \right) + \Delta t \int_{\mathbb{T}} \phi \, c_s^2 \, (V_{,X})_{n+1/2}^{(i+1)} \\ & + \Delta t \int_{\mathbb{T}} \phi_{,X} \, \tilde{\tau} c_s^2 \left(V_{n+1}^{(i+1)} - V_n + \Delta t (P_{,X})_{n+1/2}^{(i)} \right) \\ & + \Delta t \int_{\mathbb{T}} \phi_{,X} \, \nu \, (P_{,X})_{n+1/2}^{(i)} \,, \end{aligned} \tag{14}$$

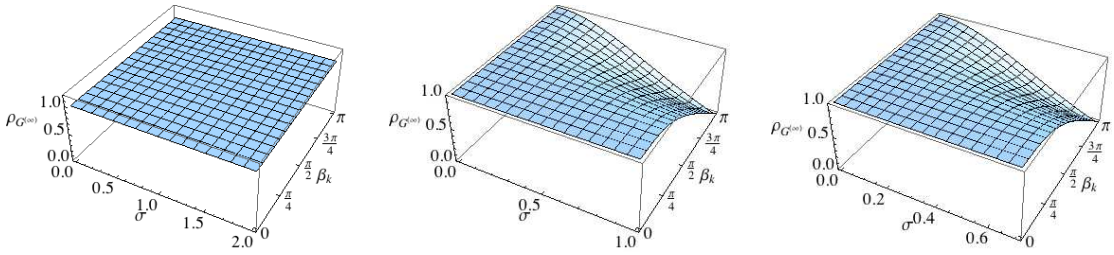

(a) $c_\tau = 0$, implicit. (b) $c_\tau = 1$, implicit. (c) $c_\tau = 2$, implicit.

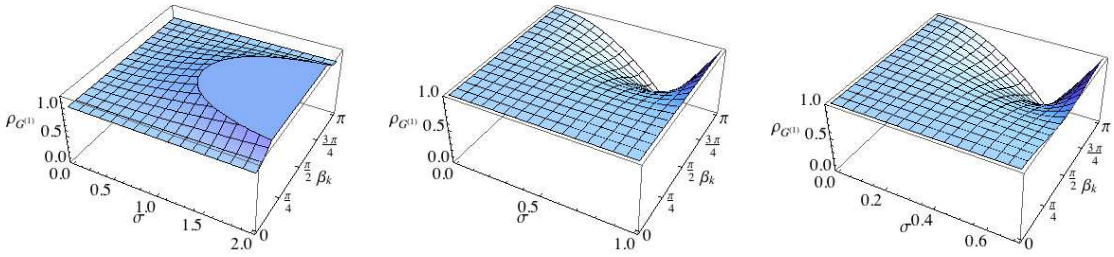

(d) $c_\tau = 0$, 1st iterate. (e) $c_\tau = 1$, 1st iterate. (f) $c_\tau = 2$, 1st iterate.

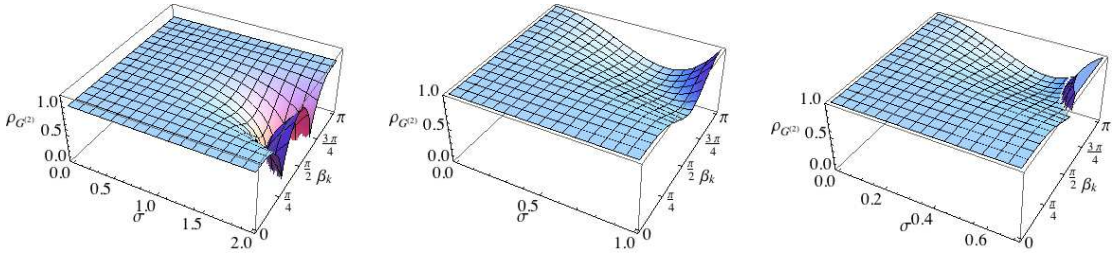

(g) $c_\tau = 0$, 2nd iterate. (h) $c_\tau = 1$, 2nd iterate. (i) $c_\tau = 2$, 2nd iterate.

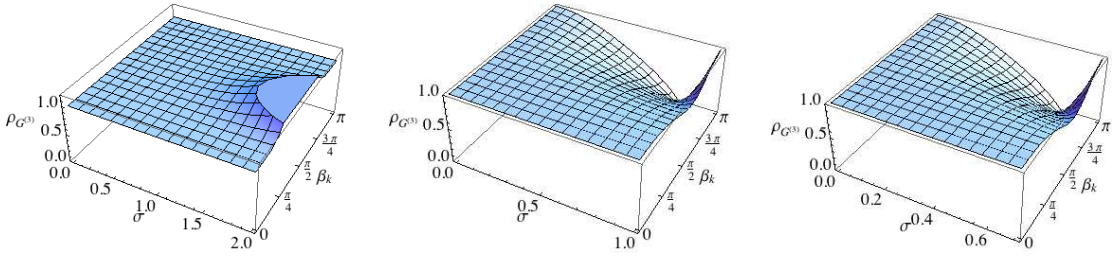

(j) $c_\tau = 0$, 3rd iterate. (k) $c_\tau = 1$, 3rd iterate. (l) $c_\tau = 2$, 3rd iterate.

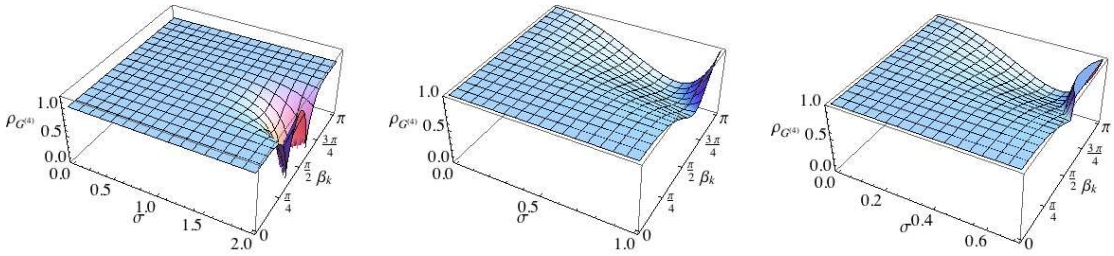

(m) $c_\tau = 0$, 4th iterate. (n) $c_\tau = 1$, 4th iterate. (o) $c_\tau = 2$, 4th iterate.

Figure 2: Elevation plots of the spectral radii $\rho_{G^{(i)}}(\sigma, \beta_k)$, for $\kappa = 0$, $c_\tau = 0, 1, 2$, and various iterates of the predictor/multi-corrector algorithm. In the top row, the implicit mid-point time integrator detailed in (39). In the subsequent rows, the iterates from one to four. For the case $c_\tau = 0$, $c_\tau = 1$, and $c_\tau = 2$, the plots are in the range $\sigma \in [0, 2]$, $\sigma \in [0, 1]$, and $\sigma \in [0, \sqrt{2}/2]$, respectively. Also, note that Figures 2(a), 2(d), 2(g), 2(j), 2(m) have a vertical range $[0, 1.2]$, while all other Figures are in the range $[0, 1]$.

where $\tilde{\tau} = \frac{\tau}{\Delta t} = \frac{c_s}{2}$, $(\cdot)^{(i)}$ and $(\cdot)^{(i+1)}$ are used to denote quantities computed with the predictor/corrector iterates (i) and $(i+1)$, respectively, and the subscripts n, $n+1$, and $n+1/2$ are used to indicate quantities at time t_n, t_n+1, and $t_{n+1/2} = (t_n + t_{n+1})/2$.

Remark1. In order to keep the analysis as close as possible to the algorithm effectively used in the computations in [12], the latest available velocity iterate is used in the computation of the second and third terms of (14). This choice yields a conservative formulation in the nonlinear extension of the algorithm, and, for this reason, this method is referred to as the *conservative* time integrator.

We assume a uniform, equispaced subdivision of the torus $\mathbb{T}$ into finite elements of measure h. As in [12], both pressure and velocity are approximated by piece-wise linear functions. Adopting mass lumping in addition to the previous assumptions, the following finite difference equations are derived:

$$\begin{aligned} 0 =& V^{(i+1)}_{j,n+1} - V_{j,n} \\ &+ \frac{\sigma}{4c_s}\left(P^{(i)}_{j+1,n+1} + P_{j+1,n} - P^{(i)}_{j-1,n+1} - P_{j-1,n}\right) \\ &- \frac{\sigma}{2c_s}\tilde{\tau}\left(P^{(i)}_{j+1,n+1} - P_{j+1,n} - P^{(i)}_{j-1,n+1} + P_{j-1,n}\right) \\ &- \frac{\kappa+\tilde{\tau}\sigma^2}{2}\left(V^{(i)}_{j+1,n+1} + V_{j+1,n} - 2V^{(i)}_{j,n+1}\right. \\ &\qquad \left. -2V_{j,n} + V^{(i)}_{j-1,n+1} + V_{j-1,n}\right), \end{aligned} \tag{15}$$

$$\begin{aligned} 0 =& P^{(i+1)}_{j,n+1} - P_{j,n} \\ &+ \frac{c_s\sigma}{4}\left(V^{(i+1)}_{j+1,n+1} + V_{j+1,n} - V^{(i+1)}_{j-1,n+1} - V_{j-1,n}\right) \\ &- \frac{c_s\sigma}{2}\tilde{\tau}\left(V^{(i+1)}_{j+1,n+1} - V_{j+1,n} - V^{(i+1)}_{j-1,n+1} + V_{j-1,n}\right) \\ &- \frac{\kappa+\tilde{\tau}\sigma^2}{2}\left(P^{(i)}_{j+1,n+1} + P_{j+1,n} - 2P^{(i)}_{j,n+1}\right. \\ &\qquad \left. -2P_{j,n} + P^{(i)}_{j-1,n+1} + P_{j-1,n}\right), \end{aligned} \tag{16}$$

where j is the node index, $\sigma = \frac{c_s\Delta t}{h}$ is the acoustic Courant number and $\kappa = \frac{\nu\Delta t}{h^2}$.

4. Von Neumann stability analysis

In conformity with the von Neumann stability analysis (see [7, 14] for details), because the boundary conditions are periodic, we can expand the solution degrees-of-freedom as a finite, linear combination of complex exponentials with complex coefficients. This eventually amounts to applying a Discrete Fourier Transform (DFT) operator to the discrete equations (15)–(16). In particular, we have:

$$V^{(i)}_{j,n} = \sum_{k=-N/2+1}^{N/2} \hat{V}^{(i)}_{k,n} e^{\mathrm{i}\beta_k j}, \tag{17}$$

$$P^{(i)}_{j,n} = \sum_{k=-N/2+1}^{N/2} \hat{P}^{(i)}_{k,n} e^{\mathrm{i}\beta_k j}, \tag{18}$$

where $\mathrm{i} = \sqrt{-1}$, and $\hat{V}^{(i)}_{k,n}$ and $\hat{P}^{(i)}_{k,n}$ are the Fourier coefficients for velocity and pressure, relative to the kth harmonic, the nth time step and the ith iterate. Note that N is the number of elements (a multiple of 2), and $\beta_k = \frac{2\pi hk}{|\mathbb{T}|} = \frac{2\pi k}{N}$ is an angularly scaled version of the integer wave number k (with $|\mathbb{T}| = \mathrm{meas}(\mathbb{T}) = Nh = 1$ the measure of the torus). Complex exponentials associated to different wave numbers satisfy a discrete orthogonality property:

$$\sum_{m=-N/2}^{N/2-1} e^{\mathrm{i}\beta_k m} e^{\mathrm{i}\beta_q m} = \delta_{kq}, \quad \text{for } -N/2 \le k, q \le N/2, \tag{19}$$

with δ_{kq} the Kronecker delta tensor ($\delta_{kq} = 1$ if $k = q$, and $\delta_{kq} = 0$ if $k \neq q$). We then replace (17)-(18) into (15)-(16) multiplied by $e^{\mathrm{i}\beta_q j}$ and $e^{\mathrm{i}\beta_r j}$, respectively, and we sum over j. Due to the orthogonality property (19), and the linearity of the system of equations (15)-(16), it is easy to verify that the previous steps lead to N pairs of equations, coupling the dynamics of the kth pressure and velocity modes, with $-N/2+1 \le k \le N/2$. Namely:

$$(\boldsymbol{I} + \boldsymbol{A}_0)\hat{\boldsymbol{Z}}^{(i+1)}_{k,n+1} = \boldsymbol{A}_1\hat{\boldsymbol{Z}}^{(i)}_{k,n+1} + (\boldsymbol{I} + \boldsymbol{A}_2)\hat{\boldsymbol{Z}}_{k,n}, \tag{20}$$

where

$$\hat{\boldsymbol{Z}}^{(i)}_{k,n} = \begin{Bmatrix} \hat{V}^{(i)}_{k,n} \\ \hat{P}^{(i)}_{k,n} \end{Bmatrix} \tag{21}$$

is the kth velocity/pressure modal pair, relative to the nth time step and the ith iterate, and

$$\boldsymbol{I} = \begin{bmatrix} 1 & 0 \\ 0 & 1 \end{bmatrix}, \tag{22}$$

$$\boldsymbol{A}_0 = \begin{bmatrix} 0 & 0 \\ -\mathrm{i}\left(\tilde{\tau} - \frac{1}{2}\right) c_s\,\sigma\sin(\beta_k) & 0 \end{bmatrix}, \tag{23}$$

$$\boldsymbol{A}_1 = \begin{bmatrix} (\tilde{\tau}\sigma^2 + \kappa)\,(\cos(\beta_k) - 1) & \mathrm{i}\left(\tilde{\tau} - \frac{1}{2}\right)\frac{\sigma}{c_s}\sin(\beta_k) \\ 0 & (\tilde{\tau}\sigma^2 + \kappa)\,(\cos(\beta_k) - 1) \end{bmatrix}, \tag{24}$$

$$\boldsymbol{A}_2 = \begin{bmatrix} (\tilde{\tau}\sigma^2 + \kappa)\,(\cos(\beta_k) - 1) & -\mathrm{i}\left(\tilde{\tau} + \frac{1}{2}\right)\frac{\sigma}{c_s}\sin(\beta_k) \\ -\mathrm{i}\left(\tilde{\tau} + \frac{1}{2}\right) c_s\,\sigma\sin(\beta_k) & (\tilde{\tau}\sigma^2 + \kappa)\,(\cos(\beta_k) - 1) \end{bmatrix}. \tag{25}$$

It is also very important to observe that because the degrees-of-freedom "signal" has real values, the discrete Fourier coefficients must satisfy the complex conjugacy property

$$\hat{\boldsymbol{Z}}^{(i)}_{-k,n} = \left(\hat{\boldsymbol{Z}}^{(i)}_{k,n}\right)^*, \quad \text{for } 0 \le k \le N/2 - 1, \tag{26}$$

where $\hat{\boldsymbol{W}}^*$ indicates the complex conjugate of $\hat{\boldsymbol{W}}$ (componentwise), and, in addition, the following condition for the often called "odd ball" mode holds:

$$\hat{\boldsymbol{Z}}^{(i)}_{N/2,p} = \boldsymbol{0}. \tag{27}$$

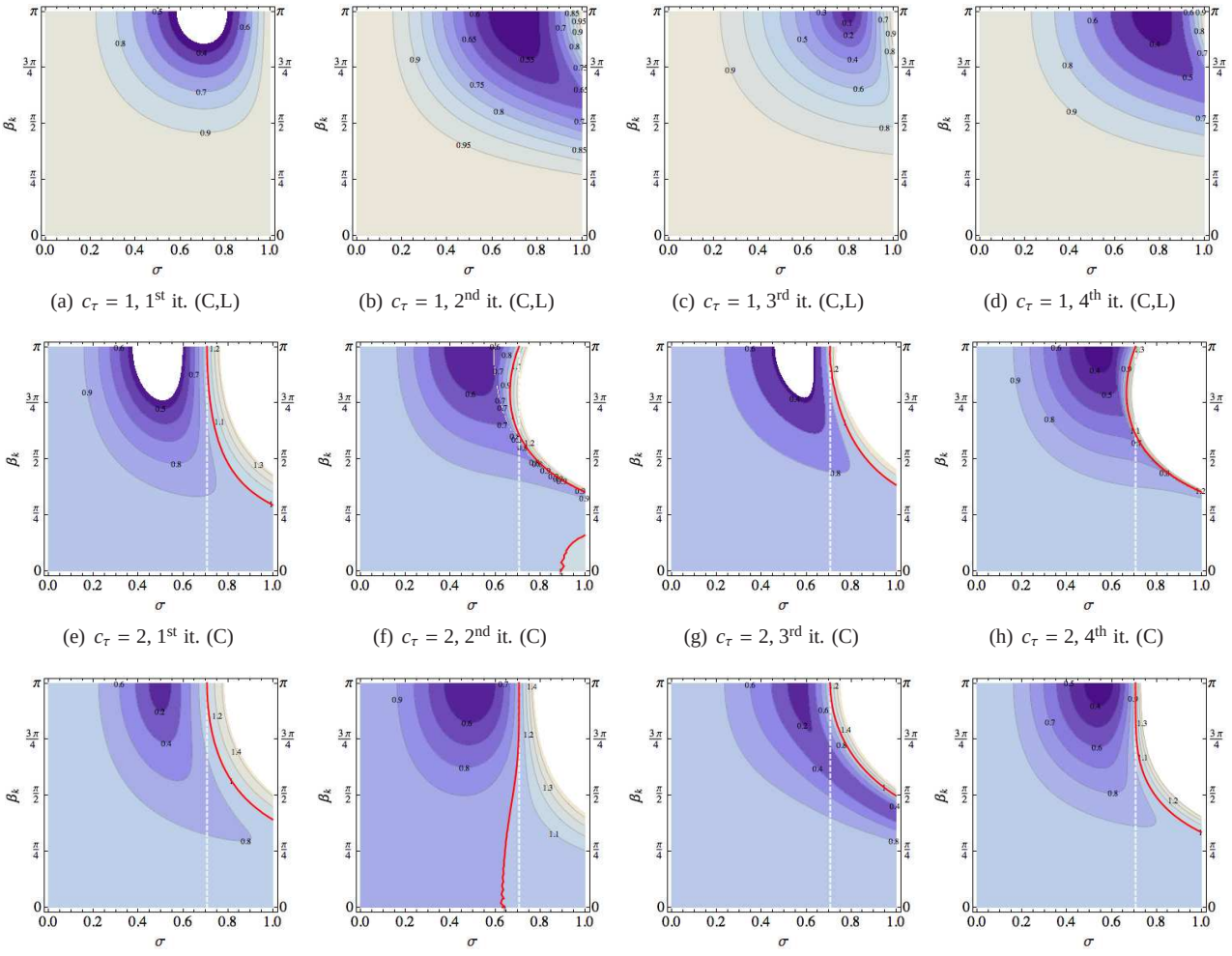

(a) $c_\tau = 1$, 1st it. (C,L) (b) $c_\tau = 1$, 2nd it. (C,L) (c) $c_\tau = 1$, 3rd it. (C,L) (d) $c_\tau = 1$, 4th it. (C,L)

(e) $c_\tau = 2$, 1st it. (C) (f) $c_\tau = 2$, 2nd it. (C) (g) $c_\tau = 2$, 3rd it. (C) (h) $c_\tau = 2$, 4th it. (C)

(i) $c_\tau = 2$, 1st it. (L) (j) $c_\tau = 2$, 2nd it. (L) (k) $c_\tau = 2$, 3rd it. (L) (l) $c_\tau = 2$, 4th it. (L)

Figure 3: Contour plots of the spectral radii of various iterates of the predictor/multi-corrector algorithm for $\kappa = 0$. Figures 3(a)–3(d): Conservative scheme for $c_\tau = 1$ (coincident with the lagged scheme (C,L)). Figures 3(e)–3(h): Conservative scheme for $c_\tau = 2$ (C). Figures 3(i)–3(l): Lagged scheme for $c_\tau = 2$ (L). The red continuous line is the contour line relative to a unit spectral radius, the white dashed line in Figures 3(e)–3(l) indicates the value $\sigma = \sqrt{2}/2$.

Because complex conjugates have the same absolute value and opposite phase, it is sufficient to limit the study of the amplification factors to the discrete modes in the range $0 \le k < N/2$, that is, $0 \le \beta_k < \pi$. In the discussion that follows, it will also be important to consider a variation of the time-integration algorithm, in which the velocity iterate $V^{(i+1)}$ in (16) is replaced by the previous iterate $V^{(i)}$. This method will be referred to as the *lagged* approach. In this case, equation (16) becomes

$$
\begin{aligned}
0 =& P^{(i+1)}_{j,n+1} - P_{j,n} \\
&+ \frac{c_s\sigma}{4}\left(V^{(i)}_{j+1,n+1} + V_{j+1,n} - V^{(i)}_{j-1,n+1} - V_{j-1,n}\right) \\
&- \frac{c_s\sigma}{4}\tilde{\tau}\left(V^{(i)}_{j+1,n+1} - V_{j+1,n} - V^{(i)}_{j-1,n+1} + V_{j-1,n}\right) \\
&- \frac{\kappa+\tilde{\tau}\sigma^2}{2}\left(P^{(i)}_{j+1,n+1} + P_{j+1,n} - 2P^{(i)}_{j,n+1}\right. \\
&\qquad \left. -2P_{j,n} + P^{(i)}_{j-1,n+1} + P_{j-1,n}\right) ,
\end{aligned}
\tag{28}
$$

and, consequently, $\boldsymbol{A}_0$ and $\boldsymbol{A}_1$ need to be modified as:

$$
\boldsymbol{A}_0 = \boldsymbol{0} , \tag{29}
$$

$$
\boldsymbol{A}_1 = \begin{bmatrix} (\tilde{\tau}\sigma^2+\kappa)(\cos(\beta_k)-1) & \mathrm{i}\left(\tilde{\tau}-\frac{1}{2}\right)\frac{\sigma}{c_s}\sin(\beta_k) \\ \mathrm{i}\left(\tilde{\tau}-\frac{1}{2}\right)c_s\,\sigma\sin(\beta_k) & (\tilde{\tau}\sigma^2+\kappa)(\cos(\beta_k)-1) \end{bmatrix} . \tag{30}
$$

This approach yields a more straightforward time integrator for the linearized equations, but does not extend, however, to a conservative scheme in the nonlinear case.

The vector equation (20) is a recurrence relationship between the predictor/multi-corrector iterates of the proposed time-integration approach. Set

$$
\boldsymbol{B}_0 = (\boldsymbol{I}+\boldsymbol{A}_0)^{-1}(\boldsymbol{I}+\boldsymbol{A}_2) , \tag{31}
$$

$$
\boldsymbol{B}_1 = (\boldsymbol{I}+\boldsymbol{A}_0)^{-1}\boldsymbol{A}_1 . \tag{32}
$$

Recalling that the first guess for the new iterate at time t_{n+1} is the solution at time t_n, namely $\hat{\boldsymbol{Z}}^{(0)}_{k,n+1} = \hat{\boldsymbol{Z}}_{k,n}$, we can derive

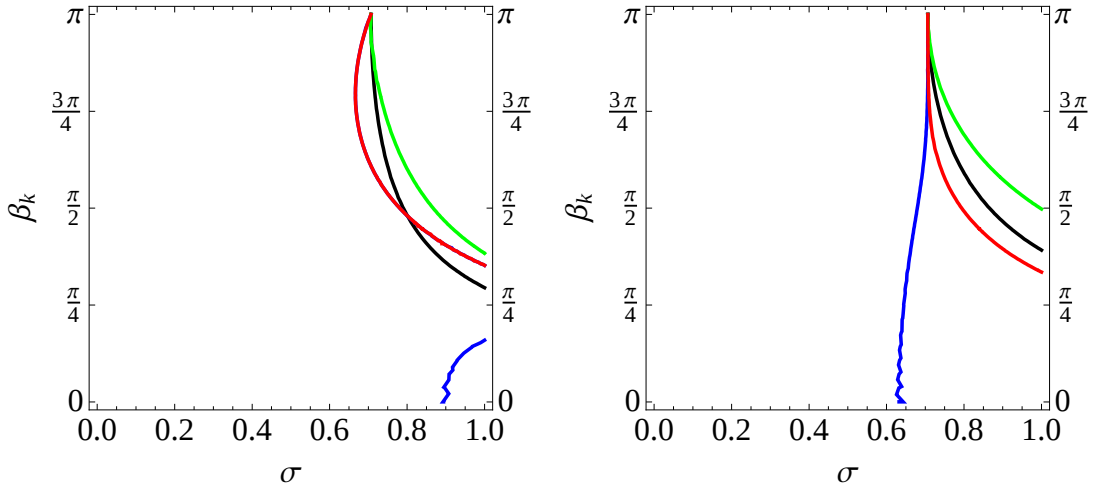

(a) $c_\tau = 2$, all iterates (C)

(b) $c_\tau = 2$, all iterates (L)

Figure 4: Contours of unit spectral radii (stability limit) for the case $c_\tau = 2$ for the conservative algorithm (Fig. 4(a)) and for the lagged algorithm (Fig. 4(b)). The color scheme is as follows: First iterate in black, second iterate in blue, third iterate in green, fourth iterate in red. In Figure 4(a), part of the curve relative to the second iterate is not visible, as it overlaps with the one relative to the fourth iterate.

explicit recurrence formulas for the computation of $\hat{\boldsymbol{Z}}^{(i+1)}_{k,n+1}$ in terms of $\hat{\boldsymbol{Z}}_{k,n}$:

$$\begin{aligned}\hat{\boldsymbol{Z}}^{(1)}_{k,n+1} &= \boldsymbol{B}_1\hat{\boldsymbol{Z}}^{(0)}_{k,n+1} + \boldsymbol{B}_0\hat{\boldsymbol{Z}}_{k,n}\\ &= (\boldsymbol{B}_0 + \boldsymbol{B}_1)\hat{\boldsymbol{Z}}_{k,n}\\ &= \boldsymbol{G}^{(1)}\hat{\boldsymbol{Z}}_{k,n}\ ,\end{aligned} \tag{33}$$

$$\begin{aligned}\hat{\boldsymbol{Z}}^{(2)}_{k,n+1} &= \boldsymbol{B}_1\hat{\boldsymbol{Z}}^{(1)}_{k,n+1} + \boldsymbol{B}_0\hat{\boldsymbol{Z}}_{k,n}\\ &= \left(\boldsymbol{B}_1\boldsymbol{G}^{(1)} + \boldsymbol{B}_0\right)\hat{\boldsymbol{Z}}_{k,n}\\ &= \boldsymbol{G}^{(2)}\hat{\boldsymbol{Z}}_{k,n}\ ,\end{aligned} \tag{34}$$

$$\begin{aligned}\hat{\boldsymbol{Z}}^{(3)}_{k,n+1} &= \boldsymbol{B}_1\hat{\boldsymbol{Z}}^{(2)}_{k,n+1} + \boldsymbol{B}_0\hat{\boldsymbol{Z}}_{k,n}\\ &= \left(\boldsymbol{B}_1\boldsymbol{G}^{(2)} + \boldsymbol{B}_0\right)\hat{\boldsymbol{Z}}_{k,n}\\ &= \boldsymbol{G}^{(3)}\hat{\boldsymbol{Z}}_{k,n}\ ,\end{aligned} \tag{35}$$

$$\begin{aligned}\hat{\boldsymbol{Z}}^{(4)}_{k,n+1} &= \boldsymbol{B}_1\hat{\boldsymbol{Z}}^{(3)}_{k,n+1} + \boldsymbol{B}_0\hat{\boldsymbol{Z}}_{k,n}\\ &= \left(\boldsymbol{B}_1\boldsymbol{G}^{(3)} + \boldsymbol{B}_0\right)\hat{\boldsymbol{Z}}_{k,n}\\ &= \boldsymbol{G}^{(4)}\hat{\boldsymbol{Z}}_{k,n}\ ,\end{aligned} \tag{36}$$

$$\hat{\boldsymbol{Z}}^{(5)}_{k,n+1} = \dots \tag{37}$$

In the limit for an infinite number of iterations, we obtain the amplification matrix for the original implicit mid-point algorithm from which the predictor/corrector time integrator is derived:

$$(\boldsymbol{I} + \boldsymbol{A}_0)\hat{\boldsymbol{Z}}^{(\infty)}_{k,n+1} = \boldsymbol{A}_1\hat{\boldsymbol{Z}}^{(\infty)}_{k,n+1} + (\boldsymbol{I} + \boldsymbol{A}_2)\hat{\boldsymbol{Z}}_{k,n}\ , \tag{38}$$

that is, removing the superscript (∞) from $\hat{\boldsymbol{Z}}^{(\infty)}_{k,n+1}$, and rearranging terms,

$$\begin{aligned}\hat{\boldsymbol{Z}}_{k,n+1} &= (\boldsymbol{I} + \boldsymbol{A}_0 - \boldsymbol{A}_1)^{-1}(\boldsymbol{I} + \boldsymbol{A}_2)\ \hat{\boldsymbol{Z}}_{k,n}\\ &= \boldsymbol{G}^{(\infty)}\hat{\boldsymbol{Z}}_{k,n}\ .\end{aligned} \tag{39}$$

Remark2. The predictor/multi-corrector method can therefore be interpreted as a fixed-point iterative process, converging to the solution of the implicit method (39). In particular, the conservative scheme has the nature of a Gauss-Seidel iteration, as the matrix $\boldsymbol{I} + \boldsymbol{A}_0$ is lower diagonal, while the lagged scheme resembles a Jacobi iteration, since $\boldsymbol{A}_0 = \boldsymbol{0}$.

Remark3. Convergence of the fixed-point iteration is ensured if $\|\boldsymbol{B}_1\| < 1$ (sufficient condition). It will be subsequently shown that this condition is equivalent to the temporal stability condition.

It is possible to evaluate the stability properties of the proposed predictor/multi-corrector algorithm, by evaluating how $\boldsymbol{G}^{(i)}$ evolves in time an initial condition. In particular, if

$$\|\boldsymbol{G}^{(i)}\| = \max_{\boldsymbol{s}\in\mathbb{R}^2\setminus\boldsymbol{0}} \frac{\|\boldsymbol{G}^{(i)}\boldsymbol{s}\|}{\|\boldsymbol{s}\|} \le 1 \tag{40}$$

then stability of the numerical discretization is ensured. Defining the spectral radius as

$$\rho(\boldsymbol{G}^{(i)}) = \max\{|\lambda(\boldsymbol{G}^{(i)})|\} \le \|\boldsymbol{G}^{(i)}\|\ , \tag{41}$$

where $\lambda(\boldsymbol{G}^{(i)})$ is a (generally complex) eigenvalue of $\boldsymbol{G}^{(i)}$, we can use slightly different condition for stability, which leads to a simpler analysis (see, e.g., [4]):

$$\rho(\boldsymbol{G}^{(i)}) < 1 \Rightarrow \text{ stability}\ , \tag{42}$$

$$\rho(\boldsymbol{G}^{(i)}) > 1 \Rightarrow \text{ instability}\ . \tag{43}$$

These conditions are consequence of a well-known theorem in matrix analysis:

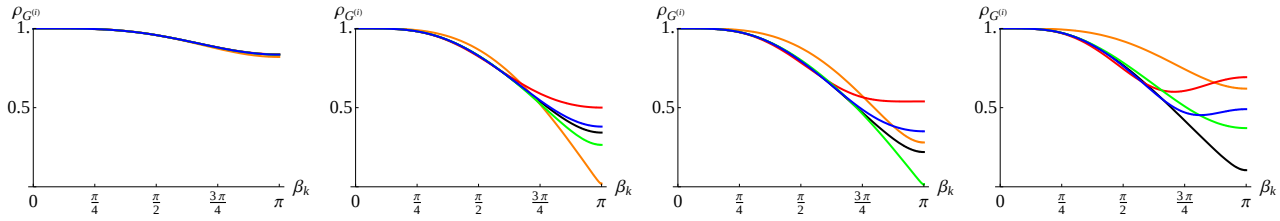

(a) $c_\tau = 1$, $\sigma = 0.3$. (C,L) (b) $c_\tau = 1$, $\sigma = 0.7$. (C,L) (c) $c_\tau = 1$, $\sigma = 0.8$. (C,L) (d) $c_\tau = 1$, $\sigma = 0.9$. (C,L)

Figure 5: Spectral radii for the stabilized predictor/multi-corrector algorithm in the case $\kappa = 0$, for various values of the acoustic Courant number σ and stabilization parameter $c_\tau = 1$, for which the conservative and lagged schemes coincide. Black: Implicit time integrator. Orange, red, green and blue are used for the first, second, third, and fourth iterates, respectively.

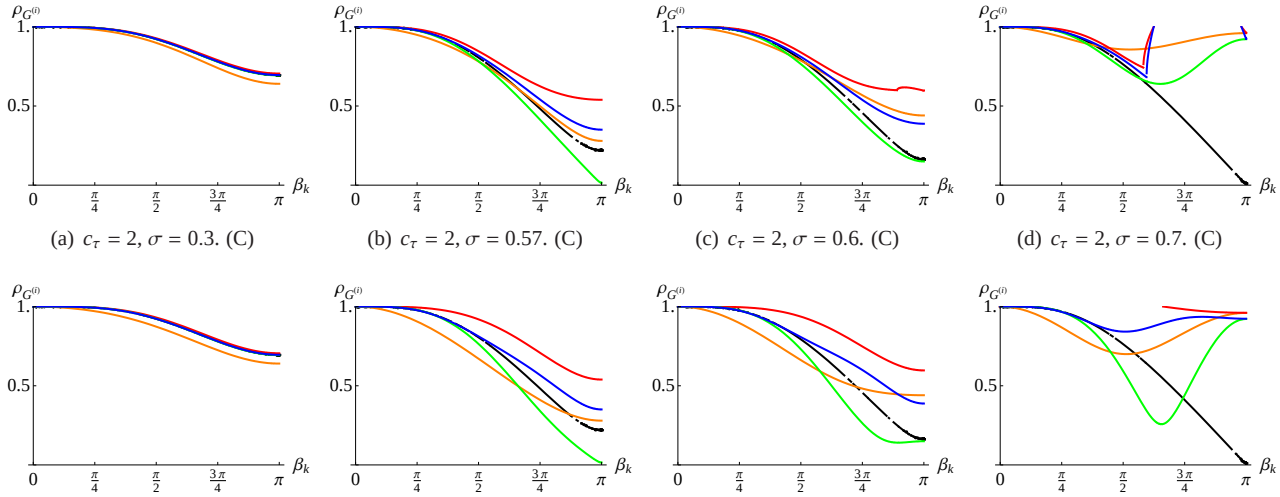

(a) $c_\tau = 2$, $\sigma = 0.3$. (C) (b) $c_\tau = 2$, $\sigma = 0.57$. (C) (c) $c_\tau = 2$, $\sigma = 0.6$. (C) (d) $c_\tau = 2$, $\sigma = 0.7$. (C)

(e) $c_\tau = 2$, $\sigma = 0.3$. (C,L) (f) $c_\tau = 2$, $\sigma = 0.57$. (C,L) (g) $c_\tau = 2$, $\sigma = 0.6$. (C,L) (h) $c_\tau = 2$, $\sigma = 0.7$. (C,L)

Figure 6: Spectral radii for the stabilized predictor/multi-corrector algorithm in the case $\kappa = 0$, for various values of the acoustic Courant number σ and stabilization parameter $c_\tau = 2$. Figures 6(a)–6(d): Conservative scheme (C). Figures 6(e)–6(h): Lagged scheme (L). Black: Implicit time integrator. Orange, red, green and blue are used for the first, second, third, and fourth iterates, respectively.

Theorem 1 (cf. [5], p. 298). *Let* $\boldsymbol{A} \in \mathbb{C}^{m\times m}$, *where* $\mathbb{C}$ *is the complex field. Then:* $\lim_{n\to\infty} \boldsymbol{A}^n = \boldsymbol{0}$ *if and only if* $\rho(\boldsymbol{A}) < 1$.

Hence, if $\rho(\boldsymbol{G}^{(i)}) < 1$, Theorem 1 directly implies stability. If $\rho(\boldsymbol{G}^{(i)}) > 1$, one can consider, as initial condition vector $\hat{\boldsymbol{Z}}_0$, the eigenvector relative to an eigenvalue λ_0 with $|\lambda_0| > 1$. Using the properties of vector norms, it is easy to see that $\lim_{n\to\infty} \|\hat{\boldsymbol{Z}}_n\| = \lim_{n\to\infty} \|(\boldsymbol{G}^{(i)})^n \hat{\boldsymbol{Z}}_0\| = \lim_{n\to\infty} |\lambda_0|^n \|\hat{\boldsymbol{Z}}_0\| = \infty$, and we have instability. The case that our analysis covers less precisely is the case when $\rho(\boldsymbol{G}^{(i)}) = 1$. Recalling that (see [5], p. 299)

$$\rho(\boldsymbol{G}^{(i)}) = \lim_{n\to\infty} \|(\boldsymbol{G}^{(i)})^n\|^{1/n} , \tag{44}$$

it is easy to realize that the case $\rho(\boldsymbol{G}^{(i)}) = 1$ admits linear growth in the solution (i.e., $\|(\boldsymbol{G}^{(i)})^n\| = O(n)$). However, the analysis that follows (see, e.g., Figures 2 and 11) shows that $\rho(\boldsymbol{G}^{(i)}) = 1$ occurs in three special cases :

1. $\sigma = 0 \Leftrightarrow \Delta t = 0$, a trivial case corresponding of no time evolution.
2. $\beta_k = 0$, corresponding to the evolution in time of a constant mode. In this case, it is not necessary to resort to the von Neumann analysis, to prove that the entire class of algorithms under consideration *stably* preserves constant solutions in time.
3. The time-step stability limit, as a limit case of the condition $\rho(\boldsymbol{G}^{(i)}) < 1$. This case is not so important in practical (nonlinear) computations, since it is usually not safe to run computations exactly at the stability limit.

Notice also that a complex eigenvalue of $\boldsymbol{G}^{(i)}$ can be expressed as:

$$\lambda(\boldsymbol{G}^{(i)}) = |\lambda(\boldsymbol{G}^{(i)})| e^{\mathrm{i}\bar{\omega}\Delta t} , \tag{45}$$

where $\bar{\omega}\Delta t = \arg(\lambda(\boldsymbol{G}^{(i)}))$, and $\bar{\omega} \in \mathbb{R}$ is the phase. This decomposition will be important for the study of the dispersion properties of the proposed time integration approach, as shown in Section 6 and Section 7. An alternative expression for (45) is

$$\lambda(\boldsymbol{G}^{(i)}) = e^{(-\bar{\xi}+\mathrm{i}\bar{\omega})\Delta t} , \tag{46}$$

where

$$|\lambda(\boldsymbol{G}^{(i)})| = e^{-\bar{\xi}\Delta t} , \qquad \text{or,} \quad \bar{\xi} = -\frac{\log(|\lambda(\boldsymbol{G}^{(i)})|)}{\Delta t} . \tag{47}$$

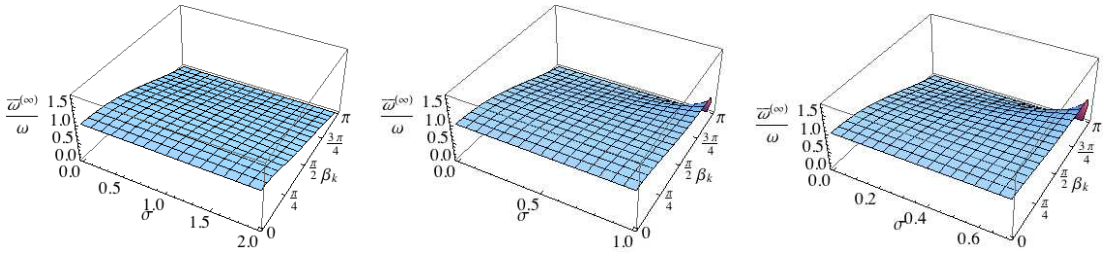

(a) $c_\tau = 0$, implicit. (b) $c_\tau = 1$, implicit. (c) $c_\tau = 2$, implicit.

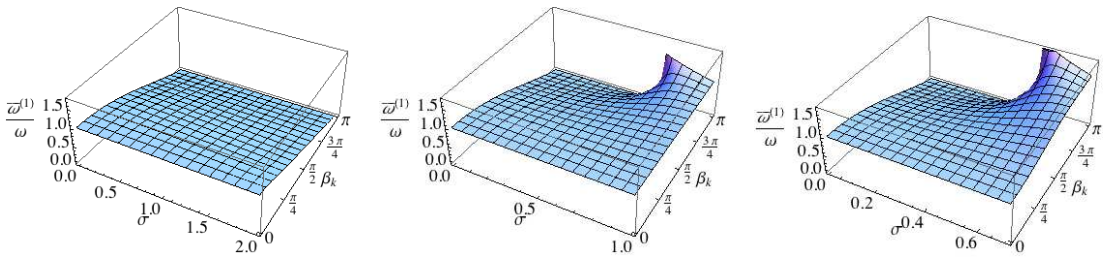

(d) $c_\tau = 0$, 1st iterate. (e) $c_\tau = 1$, 1st iterate. (f) $c_\tau = 2$, 1st iterate.

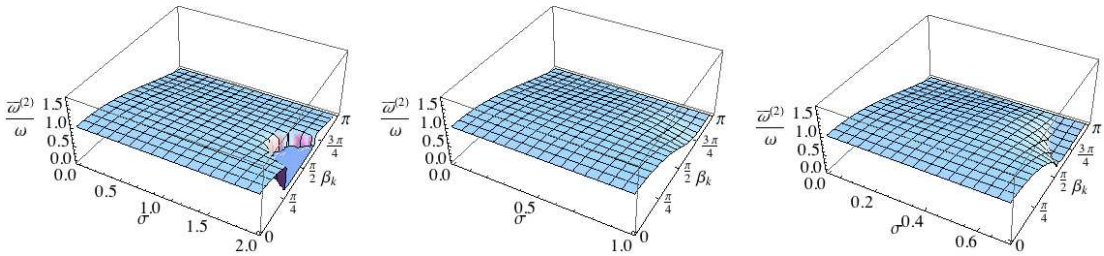

(g) $c_\tau = 0$, 2nd iterate. (h) $c_\tau = 1$, 2nd iterate. (i) $c_\tau = 2$, 2nd iterate.

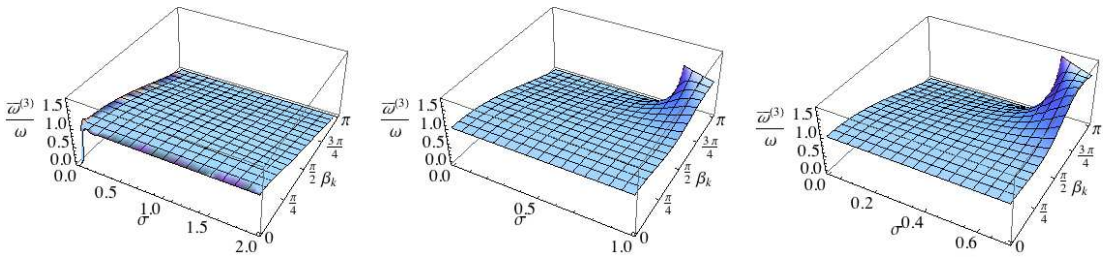

(j) $c_\tau = 0$, 3rd iterate. (k) $c_\tau = 1$, 3rd iterate. (l) $c_\tau = 2$, 3rd iterate.

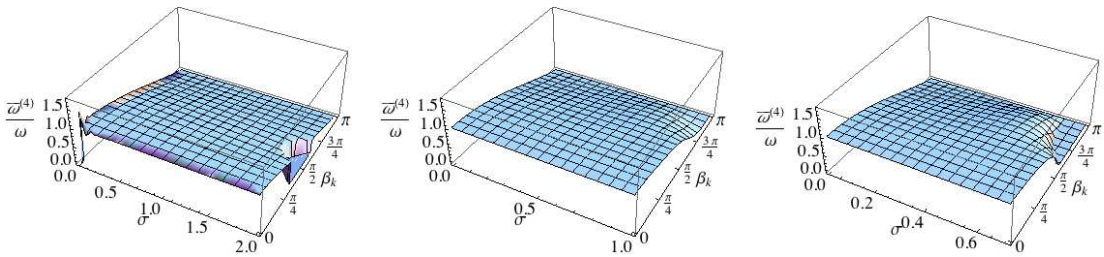

(m) $c_\tau = 0$, 4th iterate. (n) $c_\tau = 1$, 4th iterate. (o) $c_\tau = 2$, 4th iterate.

Figure 7: Elevation plots of the ratio $\bar{\omega}/\omega$, for $\kappa = 0$. Plots are for $c_\tau = 0, 1, 2$, and various iterates of the predictor/multi-corrector algorithm. In the top row, the implicit mid-point time integrator (see (39)). In the subsequent rows, the iterates from one to four. Note that for the case $c_\tau = 0$, $c_\tau = 1$, and $c_\tau = 2$, the plots are in the range $\sigma \in [0, 2]$, $\sigma \in [0, 1]$, and $\sigma \in [0, \sqrt{2}/2]$, respectively.

By performing a Taylor expansion of $\bar{\xi}$ and $\bar{\omega}$ in the limit of vanishing time step Δt and mesh size h, it is possible to recover the truncation error and the formal order of accuracy of the various iterates of the method, as shown in Section 6.3. Due to the complexity of the algebra involved, we are not including the calculations and explicit expressions of the eigenvalues of the $\boldsymbol{G}^{(i)}$ matrices. We present the fundamental results by appropriate plots in Section 6 and Section 7. All algebraic symbolic manipulations were performed using the MATHEMATICA® ™ software [1, 15].

5. Stability of the highest wavembers

Before proceeding with a complete analysis of the stability and dispersion properties of the proposed predictor/multi-corrector algorithm, it is important to develop a preliminary analysis of stability for the highest spatial wave numbers in the discrete equations. Stability of the highest modes in a computation is a necessary *but not sufficient* condition for overall stability. However, an understanding of the dynamics of high wave number modes can shed light on the overall behavior of the algorithm, and, most importantly, provide time-step control estimates of practical use in computations.

The amplification of the highest wave number is governed by the matrices $\boldsymbol{G}^{(i)}$, when β_k is set equal to π. In this case, it is easy to observe that $\boldsymbol{A}_0 = \boldsymbol{0}$, and that $\boldsymbol{A}_1$ and $\boldsymbol{A}_2$ become diagonal and equal to a multiple of the identity matrix $\boldsymbol{I}$. In particular,

$$\boldsymbol{A}_1 = \boldsymbol{A}_2 = -(c_\tau \sigma^2 + 2\kappa)\boldsymbol{I} \, . \tag{48}$$

Therefore, the time evolution of the highest pressure and velocity Fourier modes is decoupled and identical. The study of the proposed predictor/multi-corrector method can therefore be reduced to a scalar problem. Setting $\alpha = c_\tau \sigma^2 + 2\kappa \geq 0$, we obtain:

$$\boldsymbol{G}^{(1)} = (1 - 2\alpha)\boldsymbol{I} \, , \tag{49}$$

$$\boldsymbol{G}^{(2)} = (1 - 2\alpha + 2\alpha^2)\boldsymbol{I} \, , \tag{50}$$

$$\boldsymbol{G}^{(3)} = (1 - 2\alpha + 2\alpha^2 - 2\alpha^3)\boldsymbol{I} \, , \tag{51}$$

$$\boldsymbol{G}^{(4)} = (1 - 2\alpha + 2\alpha^2 - 2\alpha^3 + 2\alpha^4)\boldsymbol{I} \, , \tag{52}$$

$$\boldsymbol{G}^{(5)} = \ldots \, , \tag{53}$$

Limiting the analysis to the first four iterates, the following stability conditions are derived

$$\text{First iterate:} \quad -1 \leq 1 - 2\alpha \leq 1 \, . \tag{54}$$

$$\text{Second iterate:} \quad -1 \leq 1 - 2\alpha + 2\alpha^2 \leq 1 \, . \tag{55}$$

$$\text{Third iterate:} \quad -1 \leq 1 - 2\alpha + 2\alpha^2 - 2\alpha^3 \leq 1 \, . \tag{56}$$

$$\text{Fourth iterate:} \quad -1 \leq 1 - 2\alpha + 2\alpha^2 - 2\alpha^3 + 2\alpha^4 \leq 1 \, . \tag{57}$$

For the first iterate, the right bound yields $\alpha \geq 0$, always verified, and the left bound

$$\alpha \leq 1 \, , \tag{58}$$

which provides the time-step stability constraint. For the second iterate, the right bound yields the inequality $2\alpha(\alpha - 1) \leq 0$, which implies again the stability limit (58), while the left bound leads to the inequality $\alpha^2 - \alpha + 1 \geq 0$, always verified since the polynomial has complex roots. Hence, the first and second iterates share the same stability condition. Proceeding further, we observe that the third iterate produces a left bound given by $2 - 2\alpha + 2\alpha^2 - 2\alpha^3 = 2(1 + \alpha^2)(1 - \alpha) \geq 0$, equivalent to (58), while the right bound $-2\alpha(\alpha^2 - \alpha + 1) \leq 0$ is always verified (see the derivations for the left bound for the second iterate). The left bound for the forth iterate yields $2(1 - \alpha + \alpha^2 - \alpha^3 + \alpha^4) = 2((1 - \alpha)^4 + \alpha(3\alpha^2 - 5\alpha + 3)) \geq 0$, always verified, since the roots of the polynomial $3\alpha^2 - 5\alpha + 3$ are complex. Finally, the right bound yields $\alpha(1 + \alpha^2)(\alpha - 1) \leq 0$, again equivalent to (58). Stability limits for all remaining iterates can be obtained by recursion.

Condition (58) can then be used to estimate the stable time-step size, as it implies

$$c_\tau \sigma^2 + 2\kappa - 1 \leq 0 \, , \qquad \text{or,} \qquad c_\tau c_s^2 \Delta t^2 + 2\nu \Delta t - h^2 \leq 0 \, . \tag{59}$$

Solving the associated quadratic equation yields the bounds

$$\frac{-\nu - \sqrt{\nu^2 + c_\tau c_s^2 h^2}}{c_\tau c_s^2} \leq \Delta t \leq \frac{-\nu + \sqrt{\nu^2 + c_\tau c_s^2 h^2}}{c_\tau c_s^2} \, . \tag{60}$$

The left bound is always verified, the right gives the stability limit. Multiplying and dividing the right inequality by $\nu + \sqrt{\nu^2 + c_\tau c_s^2 h^2}$ (always a strictly positive quantity in computations) and simplifying the term $c_\tau c_s^2$, we obtain

$$\Delta t \leq \frac{h^2}{\nu + \sqrt{\nu^2 + c_\tau c_s^2 h^2}} \, . \tag{61}$$

Remark4. In the limit of a vanishing artificial viscosity, a modified advective Courant-Friedrichs-Levy condition is obtained, namely

$$\Delta t \leq \frac{h}{\sqrt{c_\tau}\, c_s} \, , \qquad \text{or,} \qquad \sigma \leq \frac{1}{\sqrt{c_\tau}} \, . \tag{62}$$

This implies that the variational multiscale stabilization is reducing the stability limit for $c_\tau > 1$ and increasing the stability limit if $c_\tau < 1$ (at least for the highest wave numbers). For $c_\tau = 1$, the standard acoustic Courant-Friedrichs-Levy stability condition is recovered.

Remark5. In the limit of a vanishing speed of sound (condition very often encountered in hypervelocity impact problems), the stability limit is uniquely dependent on the artificial viscosity ν and takes the classical form of the dissipative Courant-Friedrichs-Levy condition:

$$\Delta t \leq \frac{h^2}{2\nu} \, , \qquad \text{or,} \qquad \kappa \leq \frac{1}{2} \, . \tag{63}$$

Remark6. As already mentioned, the predictor multi-corrector approach can also be interpreted as a fixed-point iteration procedure [11]. A sufficient condition for the convergence (in spectral space) of such procedure is $\|\boldsymbol{B}_1\| < 1$, that is $\rho(\boldsymbol{B}_1) < 1$. It

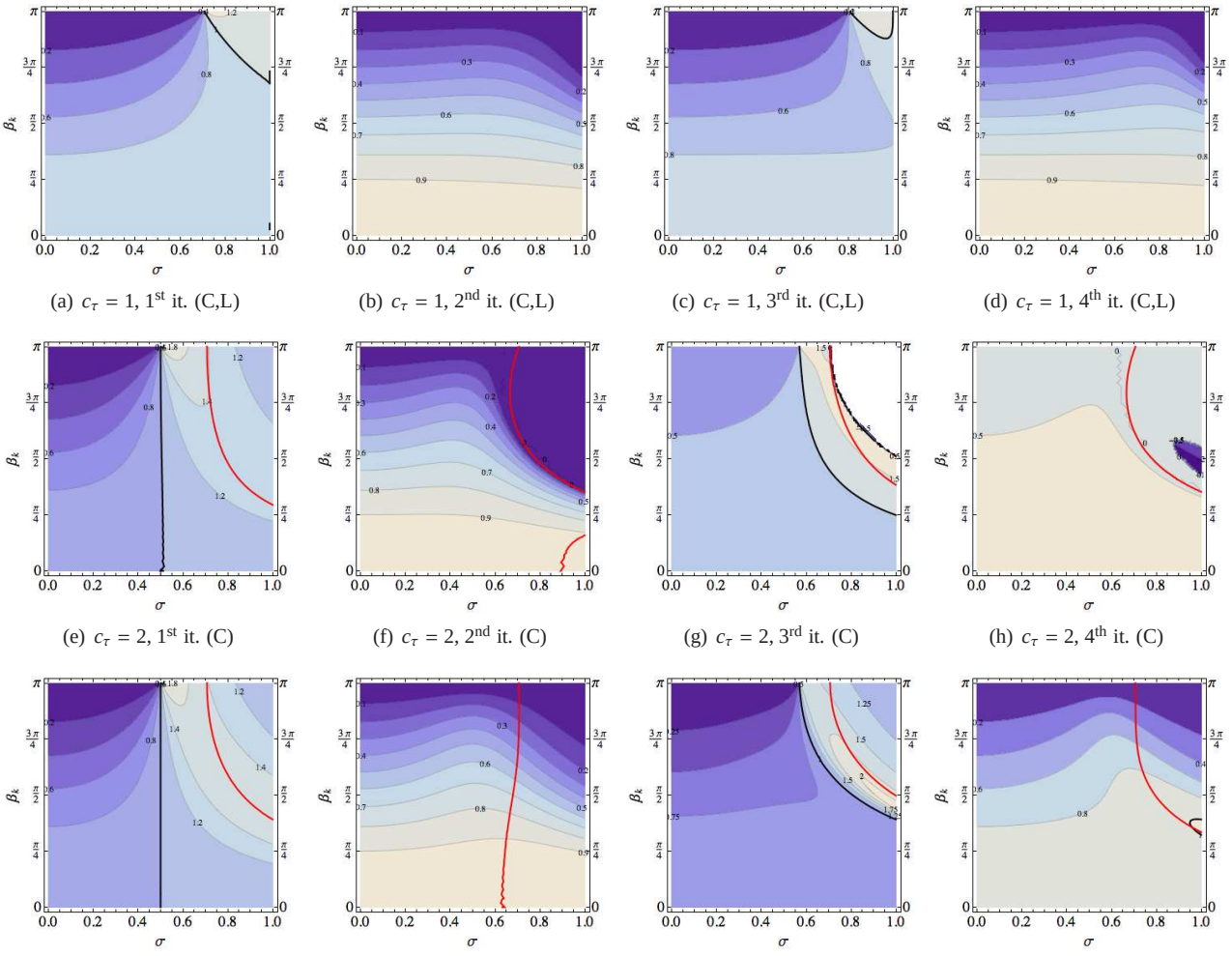

(a) $c_\tau = 1$, 1st it. (C,L) (b) $c_\tau = 1$, 2nd it. (C,L) (c) $c_\tau = 1$, 3rd it. (C,L) (d) $c_\tau = 1$, 4th it. (C,L)

(e) $c_\tau = 2$, 1st it. (C) (f) $c_\tau = 2$, 2nd it. (C) (g) $c_\tau = 2$, 3rd it. (C) (h) $c_\tau = 2$, 4th it. (C)

(i) $c_\tau = 2$, 1st it. (L) (j) $c_\tau = 2$, 2nd it. (L) (k) $c_\tau = 2$, 3rd it. (L) (l) $c_\tau = 2$, 4th it. (L)

Figure 8: Contour plots of the ratio $\bar{\omega}/\omega$, for $\kappa = 0$. Plots are for $c_\tau = 1, 2$, and various iterates of the predictor/multi-corrector algorithm. Figures 8(a)–8(d): Conservative scheme for $c_\tau = 1$ (coincident with the lagged scheme (C,L)). Figures 8(e)–8(h): Conservative scheme for $c_\tau = 2$ (C). Figures 8(i)–8(l): Lagged scheme for $c_\tau = 2$ (L). The red continuous line is the locus of a unit spectral radius. The black continuous line indicates the locus $\bar{\omega}/\omega = 1$ (no phase error).

is not difficult to verify that, in the case of the highest wave number, that is $\beta_k = \pi$, this condition coincides with (59). By plotting contour surfaces at $\rho(\boldsymbol{B}_1) = 1$, we were also able to graphically verify that the stability implies convergence of the corrector iterates on the entire space $[\sigma, \kappa, \beta_k]$. This approach is virtually identical to the one outlined in Section 7.1 (particularly, Figure 15) and will not be reported here, for the sake of brevity.

6. The case of vanishing viscosity

In shock hydrodynamics computations, the artificial viscosity is usually present only in shock layers, and is absent in expansion regions. Therefore, it is very important to study the proposed time integrator in the limit of a vanishing viscosity, as the most part of the flow domain is subject to this condition.

6.1. Amplification factor

Figure 2 shows the spectral radii of the matrices $\boldsymbol{G}^{(i)}$ for $i \to \infty$ (implicit scheme) and $i = 1, 2, 3, 4$, with stabilization parameter $c_\tau = 0, 1, 2$. First, note that the implicit algorithm detailed in (39) is neutrally stable in the case of no stabilization, as the spectral radius of the corresponding amplification matrix is equal to unity over the entire plane $[\sigma, \beta]$ (Fig. 2(a)). Without stabilization, only the *even* iterates are stable in the predictor/multi-corrector version, as detailed in Figures 2(g) and 2(m). As shown in Figures 2(d) and 2(j) (note in particular that these vertical range of the plot is $[0, 1.2]$), when stabilization is absent, the first and third iterates of the proposed algorithm are *unconditionally unstable*. This somewhat surprising phenomenon can be explained by realizing that the spectral radii for the predictor/multi-corrrector scheme exhibit a *non-monotonic* convergence to unity as $(i) \to \infty$.

When $c_\tau = 1$ the conserved and lagged variants of the stabilized algorithm coincide. The implicit case in Fig. 2(b) is stable, and the stability range for the predictor/multi-corrector is $\sigma \in [0, 1]$ (Fig. 2(e), 2(h), 2(k), and 2(n)), as predicted in Section 5. In the case $c_\tau = 2$, the stability region of some of the iterates for either the conservative or the lagged scheme does not completely extend to $\sigma = 1/\sqrt{2}$ (i.e., the stability limit for

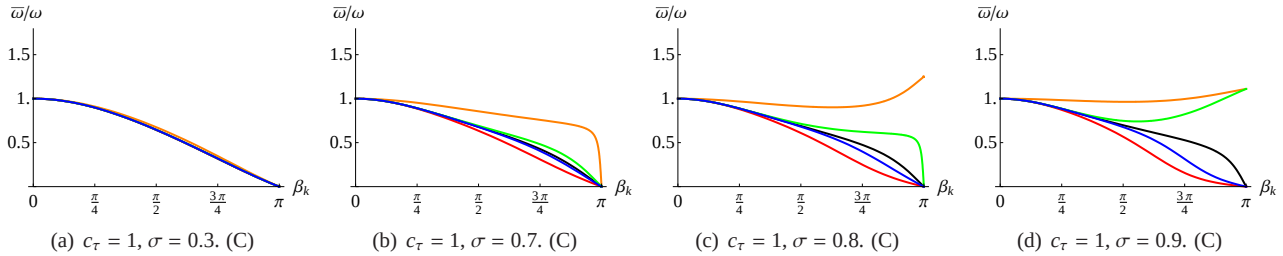

(a) $c_\tau = 1$, $\sigma = 0.3$. (C) (b) $c_\tau = 1$, $\sigma = 0.7$. (C) (c) $c_\tau = 1$, $\sigma = 0.8$. (C) (d) $c_\tau = 1$, $\sigma = 0.9$. (C)

Figure 9: Plot of the ratio $\overline{\omega}/\omega$, for $\kappa = 0$, for various values of the acoustic Courant number σ and $c_\tau = 1$, for which the conservative and lagged schemes coincide. Color scheme is as follows. Black: Implicit time integrator. Orange, red, green and blue are used for the first, second, third, and fourth iterate, respectively.

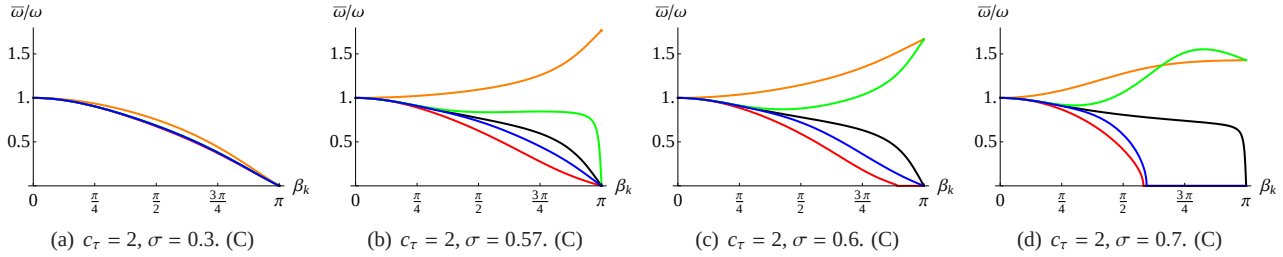

(a) $c_\tau = 2$, $\sigma = 0.3$. (C) (b) $c_\tau = 2$, $\sigma = 0.57$. (C) (c) $c_\tau = 2$, $\sigma = 0.6$. (C) (d) $c_\tau = 2$, $\sigma = 0.7$. (C)

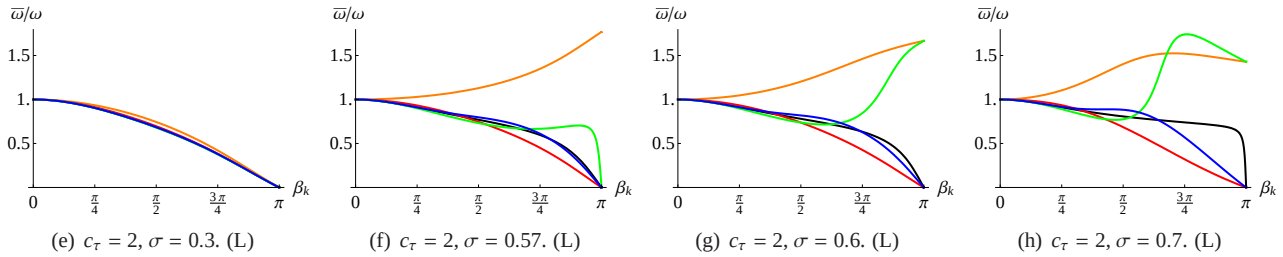

(e) $c_\tau = 2$, $\sigma = 0.3$. (L) (f) $c_\tau = 2$, $\sigma = 0.57$. (L) (g) $c_\tau = 2$, $\sigma = 0.6$. (L) (h) $c_\tau = 2$, $\sigma = 0.7$. (L)

Figure 10: Plot of the ratio $\overline{\omega}/\omega$, for $\kappa = 0$, for various values of the acoustic Courant number σ and $c_\tau = 2$. Figures 10(a)–10(d): Conservative scheme (C). Figures 10(e)–10(h): Lagged scheme (L). Color scheme is as follows. Black: Implicit time integrator. Orange, red, green and blue are used for the first, second, third, and fourth iterate, respectively.

the highest wave numbers, derived in Section 5). This feature is the result of the increased value of the stabilization constant, which causes some of the lower modes to go unstable before the highest. Observe that, in this case, the range of stability is a function of the number of iterations of the predictor/multi-corrector. In fact, the first and third iterates of the conservative scheme (Figs. 3(e) and 3(g)) are stable over the entire range $\sigma \in [0, 1/\sqrt{2}]$, as well as the first, third and forth iterates of the lagged scheme (Figs. 3(i), 3(k), and 3(l)). Figure 4 shows the stability isolines at which the spectral radii of various amplification matrices are unity, when $c_\tau = 2$. In the case of the conservative algorithm in Figure 4(a), it is easy to realize that introducing a safety factor 0.9 is sufficient in recovering a stability range for all iterates, namely $\sigma \in [0, 0.9/\sqrt{2}]$.

Additional information can be gained by plotting sections of the spectral radius elevation plots of the various amplification matrices for different values of the acoustic Courant number σ, as shown in Figures 5 and 6. Figures 5(a)–5(d) show the results for the coinciding conservative and lagged schemes with $c_\tau = 1$, Figures 6(a)–6(d) show results for the conservative scheme with $c_\tau = 2$, while Figures 6(e)–6(h) show results for the lagged scheme, again with $c_\tau = 2$. Observe that high wave number damping increases as the value of c_τ increases. It is also easily appreciated the convergence of the spectral radii of the iterates to the spectral radii of the corresponding implicit schemes, represented by black lines. In Figure 6(c), it is visible the onset of a bifurcation point for the amplification matrix of the second iterate (the kink in the red curve near $\beta_k = 7\pi/8$). This phenomenon is more clearly visible in Figure 6(d), a section of the spectral radii *past* the stability limit $0.9/\sqrt{2} \approx 0.64$, for the second and fourth iterates (the red and blue curves in proximity of $\beta_k = 5\pi/8$). Past a bifurcation point, the eigenvalues of the corresponding amplification matrix cease to be complex conjugate, as evident in Figures 10(c) and 10(d), by the absence of a phase in the eigenvalues. This is not a desirable property in discretized wave propagation problems which should behave as systems of harmonic oscillators. In [12], the best numerical results in terms of accuracy and robustness (low mesh distortion) were obtained with three iterates of the conservative algorithm, $c_\tau = 2$ and a safety factor 0.8 (i.e., $\sigma = 0.8/\sqrt{2} \approx 0.57$). This choices correspond to the green curve in Figure 6(b): The high wave number damping, the moderate low wave number error, and the absence of an eigenvalue bifurcation explains these findings.

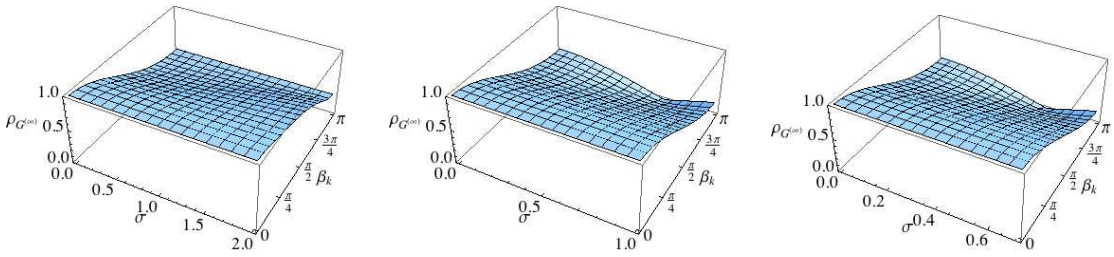

(a) $c_\tau = 0$, implicit. (b) $c_\tau = 1$, implicit. (c) $c_\tau = 2$, implicit.

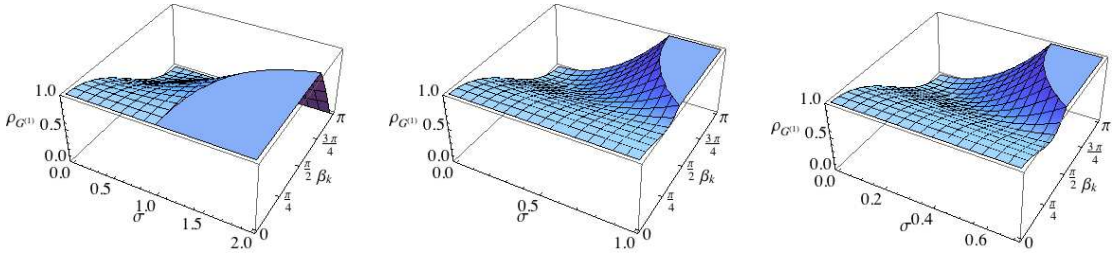

(d) $c_\tau = 0$, 1st iterate. (e) $c_\tau = 1$, 1st iterate. (f) $c_\tau = 2$, 1st iterate.

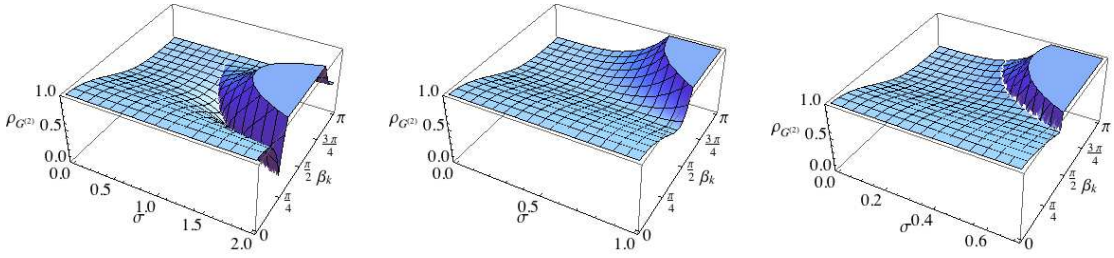

(g) $c_\tau = 0$, 2nd iterate. (h) $c_\tau = 1$, 2nd iterate. (i) $c_\tau = 2$, 2nd iterate.

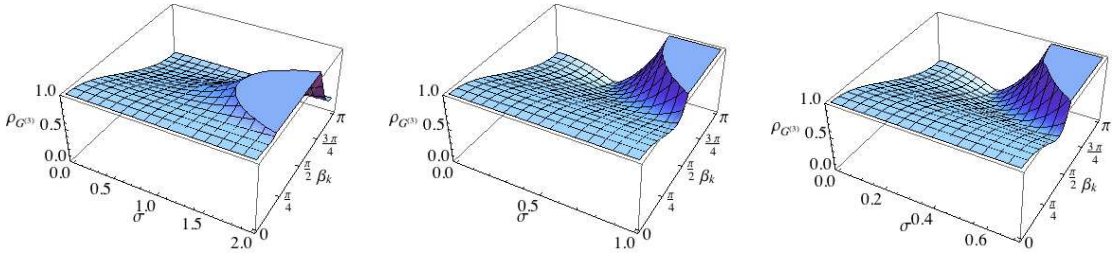

(j) $c_\tau = 0$, 3rd iterate. (k) $c_\tau = 1$, 3rd iterate. (l) $c_\tau = 2$, 3rd iterate.

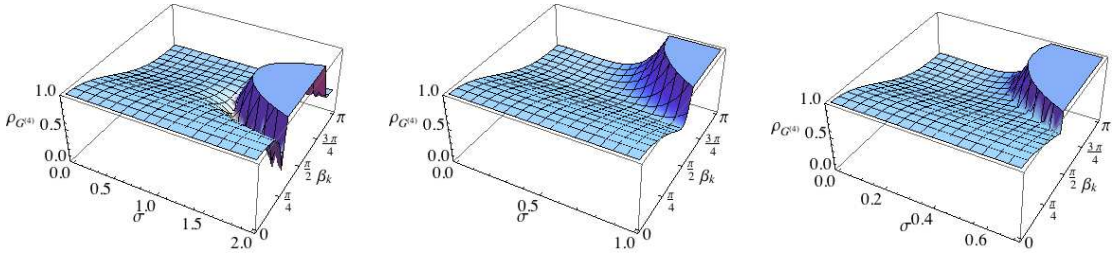

(m) $c_\tau = 0$, 4th iterate. (n) $c_\tau = 1$, 4th iterate. (o) $c_\tau = 2$, 4th iterate.

Figure 11: Elevation plots of the spectral radii $\rho_{G^{(i)}}$, for $\kappa = 1/4$. Plots are for $c_\tau = 0, 1, 2$, and various iterates of the predictor/multi-corrector algorithm. In the top row, the implicit mid-point time integrator (see (39)). In the subsequent rows, the iterates from one to four. The spectral radii are presented as a function of σ and β_k. Note that for the case $c_\tau = 0$, $c_\tau = 1$, and $c_\tau = 2$, the plots are in the range $\sigma \in [0, 2]$, $\sigma \in [0, 1]$, and $\sigma \in [0, \sqrt{2}/2]$, respectively.

6.2. Dispersion error

When no viscosity is present, it is very insighful to evaluate the extent of the dispersion error in computations. For this purpose, observe that the classical dispersion relationship for a linear wave is given by $\omega = 2\pi k c_s/|\mathbb{T}|$. Recalling that $|\mathbb{T}| = hN$, it is easily derived

$$\omega \Delta t = \sigma \beta_k \ . \tag{64}$$

A typical measure of the dispersion error is given by the ratio

$$\frac{\bar{\omega}}{\omega} = \frac{\arg(\lambda(\sigma, \beta_k))}{\sigma \beta_k} \ . \tag{65}$$

When $\bar{\omega}/\omega = 1$, no dispersion error is present for a certain wave number β_k at a certain value of σ. Figure 7 shows elevation plots of the ratio $\bar{\omega}/\omega$. It is noticeable in Figures 7(g) and 7(m) that eigenvalue bifurcation takes place for values of $[\sigma, \beta_k] \approx [2, \pi/2]$, when no stabilization is applied. Although less notably, this also occurs for the conservative stabilized case with $c_\tau = 2$ (Figs. 7(i), and 7(o)), for $[\sigma, \beta_k]$ near $[1, \pi/2]$, as already mentioned in Section 6.1. Contour plots of the dispersion ratio are presented in Figure 8. The black thick lines indicate the loci where the dispersion ratio equals unity. The red thick lines indicate the locus of the amplification factor equal to unity (i.e., the stability limit). Note that the predictor/multi-corrector iterates show degradation of the phase error in proximity of the stability limits, with respect to the corresponding implicit algorithms (see also Fig. 7). The noticeable "distortion" in the contour lines near the stability boundary indicates a significant growth in the phase errors. However, the third iterate for the stabilized case for $c_\tau = 1$ and $c_\tau = 2$ shows fairly moderate phase error for $\sigma \in [0.8, 0.9]$ and $\sigma = 0.57$, respectively, as seen in Figures 9 and 10.

Remark7. Computations documented in [12] using $c_\tau = 2$ were most often performed at $\sigma = 0.8/\sqrt{c_\tau} \approx 0.57$ with three iterates of the predictor/multi-corrector. This choice corresponds to high wave number damping and small overall phase error (see also Fig. 6(b)), and was found in [12] to reduce mesh distortion in blast tests of Sedov type [13].

Remark8. The fact that the variational multiscale stabilization with $c_\tau = 2$ reduces by a factor $1/\sqrt{2}$ the stability limit should not be considered as an indication that the variational multiscale shock hydrodynamics method would require 30% more time steps than a standard hydrocode computation. In fact, the opposite can be said: A comparison on multidimensional tests showed that the variational multiscale method required on average 20-30% fewer time steps than the more standard constant pressure finite element implementation in [11]. This is due to the fact that the proposed variational multiscale approach provides considerable reduction in mesh distortion with respect to a standard hydrocode implementation, with very positive effects also on the overall time advancement constraint.

In Figures 7 and 8, it is noticeable the difference in behavior between the odd and even iterates of the method. Restricting our analysis to the stabilized case, we see that odd iterates overshoot the frequency ω for high values of β_k and σ, while even iterates undershoot the frequency in the same range of values for β_k and σ. This is most clearly appreciated in Figure 9 and 10.

6.3. Low wave number limit and truncation error

A Taylor expansion of the amplification factor ρ and dispersion ratio $\bar{\omega}/\omega$ in a right neighborhood of $\beta_k = 0$ can more clearly quantify the previous conclusions on the nature of the proposed conservative algorithm. We consider only the conservative algorithm, and we obtain, for the amplification factor

$$\rho(\boldsymbol{G}^{(1)}_{c_\tau=1}) = 1 - \sigma^2 \left(\frac{1}{6} - \frac{\sigma^2}{8} \right) \beta_k^4 + O(\beta_k^6) \ , \tag{66}$$

$$\rho(\boldsymbol{G}^{(2,3,4,\ldots,\infty)}_{c_\tau=1}) = 1 - \sigma^2 \left(\frac{1}{6} + \frac{\sigma^2}{8} \right) \beta_k^4 + O(\beta_k^6) \ , \tag{67}$$

and

$$\rho(\boldsymbol{G}^{(1)}_{c_\tau=2}) = 1 - \frac{\sigma^2}{4} \beta_k^2 + O(\beta_k^4) \ , \tag{68}$$

$$\rho(\boldsymbol{G}^{(2,3,4,\ldots,\infty)}_{c_\tau=2}) = 1 - \sigma^2 \left(\frac{1}{6} + \frac{\sigma^2}{8} \right) \beta_k^4 + O(\beta_k^6) \ . \tag{69}$$

Therefore, the stabilized method is always stable for low wave numbers. Note also that the leading terms in the Taylor expansions are identical for both $c_\tau = 1$ and $c_\tau = 2$, for a number of iteration larger than or equal to two. The expansions also suggest that the method for $c_\tau = 1$ is always second order in time, while the method for $c_\tau = 2$ is first order for the first iterate and second from the second iterate on. The expansions for the phase show a similar trend, namely:

$$\frac{\bar{\omega}(\boldsymbol{G}^{(1)}_{c_\tau=1})}{\omega} = 1 - \frac{1 - \sigma^2}{6} \beta_k^2 + O(\beta_k^4) \ , \tag{70}$$

$$\frac{\bar{\omega}(\boldsymbol{G}^{(2,3,4,\ldots,\infty)}_{c_\tau=1})}{\omega} = 1 - \sigma^2 \left(\frac{1}{6} + \frac{\sigma^2}{12} \right) \beta_k^2 + O(\beta_k^4) \ , \tag{71}$$

and

$$\frac{\bar{\omega}(\boldsymbol{G}^{(1)}_{c_\tau=2})}{\omega} = 1 - \frac{16 - 61\sigma^2}{96} \beta_k^2 + O(\beta_k^4) \ , \tag{72}$$

$$\frac{\bar{\omega}(\boldsymbol{G}^{(2,3,4,\ldots,\infty)}_{c_\tau=2})}{\omega} = 1 - \sigma^2 \left(\frac{1}{6} + \frac{\sigma^2}{12} \right) \beta_k^2 + O(\beta_k^4) \ , \tag{73}$$

which suggest that both stabilized methods are second-order accurate for the phase. More precise information can be gained by means of a double Taylor series expansion of $\bar{\xi}$ and $\bar{\omega}$ in powers of the time step Δt and mesh spacing h. When $c_\tau = 1$ we obtain

$$\bar{\xi}(\boldsymbol{G}^{(1)}_{c_\tau=1}) = \frac{c_s^2 \tilde{k}^4}{8} h^2 \, \Delta t - \frac{c_s^4 \tilde{k}^4}{8} \Delta t^3 + O(h^4 \Delta t, \Delta t^3 h^2) \ , \tag{74}$$

$$\bar{\xi}(\boldsymbol{G}^{(2,3,4,\ldots,\infty)}_{c_\tau=1}) = \frac{c_s^2 \tilde{k}^4}{8} h^2 \, \Delta t + O(\Delta t \, h^4, \Delta t^3 h^2) \ , \tag{75}$$

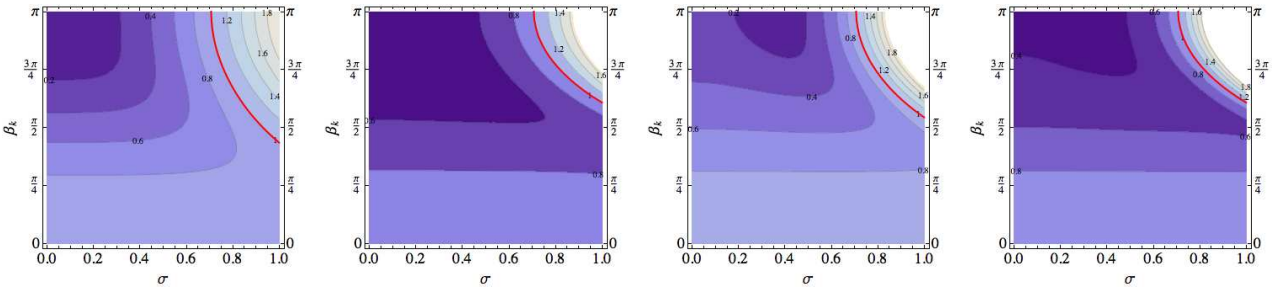

(a) $c_\tau = 1$, 1st iterate. (b) $c_\tau = 1$, 2nd iterate. (c) $c_\tau = 1$, 3rd iterate. (d) $c_\tau = 1$, 4th iterate.

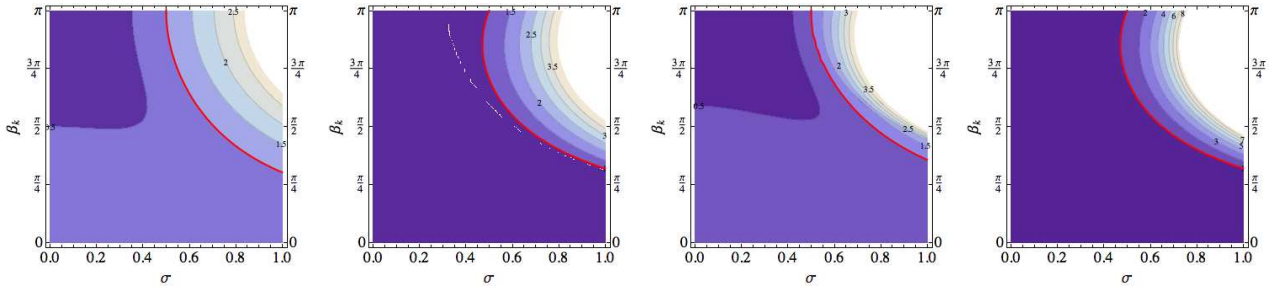

(e) $c_\tau = 2$, 1st iterate. (f) $c_\tau = 2$, 2nd iterate. (g) $c_\tau = 2$, 3rd iterate. (h) $c_\tau = 2$, 4th iterate.

Figure 12: Contour plots of the spectral radii for various predictor/multi-corrector iterates of the conservative algorithm in the case $\kappa = 1/4$. Figures 3(a)–3(d) show the case of $c_\tau = 1$. Figures 3(e)–3(h) show the case of $c_\tau = 2$. The red continuous curves are isolines of unit spectral radius.

and

$$\bar{\omega}(\boldsymbol{G}^{(1)}_{c_\tau=1}) = \omega - \frac{c_s\tilde{k}^3}{6}h^2 + \frac{c_s^3\tilde{k}^3}{6}\Delta t^2 + O(\Delta t^4, \Delta t^2 h^2, h^4)\,, \tag{76}$$

$$\bar{\omega}(\boldsymbol{G}^{(2,3,4,\ldots,\infty)}_{c_\tau=1}) = \omega - \frac{c_s\tilde{k}^3}{6}h^2 - \frac{c_s^3\tilde{k}^3}{12}\Delta t^2 + O(\Delta t^4, \Delta t^2 h^2, h^4)\,, \tag{77}$$

where $\tilde{\kappa} = 2\pi k/|\mathbb{T}|$, so that $\omega = \tilde{\kappa}c_s$. We conclude that the formal order of accuracy of all the iterates of the method is third order with regard to dissipation and second order withe regard to dispersion, when Δt and h are balanced by a CFL condition. In the case $c_\tau = 2$, we obtain

$$\bar{\xi}(\boldsymbol{G}^{(1)}_{c_\tau=2}) = \frac{c_s^2\tilde{k}^2}{4}\Delta t + O(h^2\Delta t, \Delta t^3)\,, \tag{78}$$

$$\bar{\xi}(\boldsymbol{G}^{(2)}_{c_\tau=2}) = \frac{c_s^2\tilde{k}^4}{4}h^2\,\Delta t - \frac{5c_s^2\tilde{k}^4}{16}\Delta t^3 + O(\Delta t\, h^4, \Delta t^3 h^2)\,, \tag{79}$$

$$\bar{\xi}(\boldsymbol{G}^{(3,4,\ldots,\infty)}_{c_\tau=2}) = \frac{c_s^2\tilde{k}^4}{4}h^2\,\Delta t + O(\Delta t\, h^4, \Delta t^3 h^2)\,, \tag{80}$$

and

$$\bar{\omega}(\boldsymbol{G}^{(1)}_{c_\tau=2}) = \omega - \frac{c_s\tilde{k}^3}{6}h^2 + \frac{61c_s^3\tilde{k}^3}{96}\Delta t^2 + O(\Delta t^4, \Delta t^2 h^2, h^4)\,, \tag{81}$$

$$\bar{\omega}(\boldsymbol{G}^{(2,3,4,\ldots,\infty)}_{c_\tau=2}) = \omega - \frac{c_s\tilde{k}^3}{6}h^2 - \frac{c_s^3\tilde{k}^3}{12}\Delta t^2 + O(\Delta t^4, \Delta t^2 h^2, h^4)\,. \tag{82}$$

Under the assumption that the time step Δt and mesh spacing h are balanced by a CFL condition, the previous derivations imply that the dissipation error is first order for the first iterate and third order for all other iterates, while the dispersion error is second order for all iterates. Overall, the proposed stabilized method is formally second order accurate, for two or more iterations of the predictor/multi-corrector procedure. Also note that the leading term in the second iterate for $c_\tau = 2$ has not yet converged to its limit value, indicating that at least three iterations are required to exactly retain the properties of the implicit limit algorithm in the low wave number regime.

7. The case of non-vanishing viscosity

Artificial viscosity operators are usually added in shock hydrodynamics computations to enhance robustness under severe shock wave conditions. Viscosity operators usually are modeled as Laplace diffusive operators, and may pose additional constraints on stability, further limiting the time step. It is therefore important to present a thorough analysis and time-step control estimate, when dissipation is present. In this case, because of the parabolic nature of the problem, the dispersion error analysis is less relevant and will be omitted. Only results for the conservative scheme are presented.

7.1. Amplification factor

The amplification factor (spectral radius) of the matrices $\boldsymbol{G}^{(i)}$ is shown as a function of the non-dimensional wave number β_k and acoustic Courant number σ in Figure 11, for a value of the non-dimensional viscosity coefficient $\kappa = 1/4$. A comparison of Figure 11 with Figure 2 shows that the introduction of a

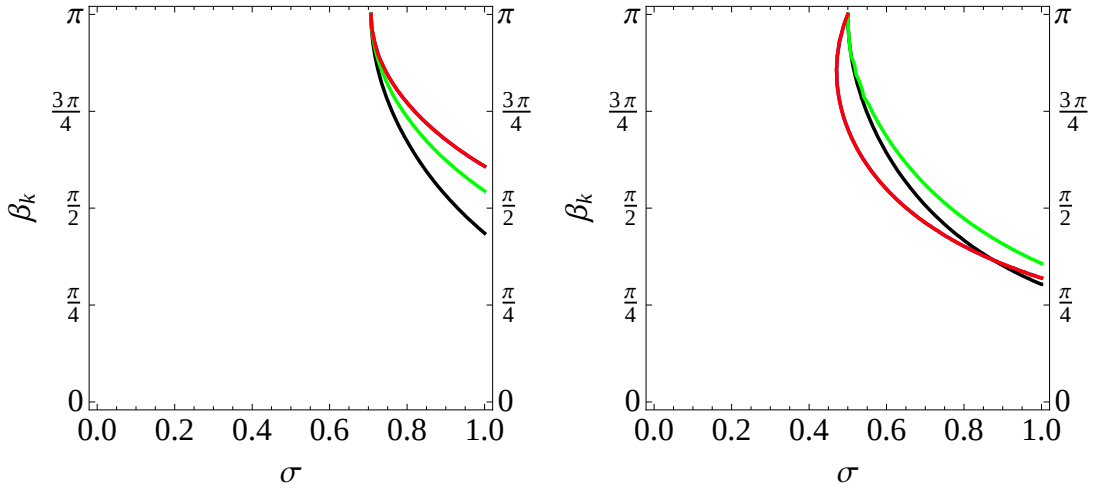

(a) $c_\tau = 1$, all iterates.

(b) $c_\tau = 2$, all iterates.

Figure 13: Contour plots of the loci of the spectral radii equal to unity for the case $c_\tau = 1$ (Fig. 13(a)) and $c_\tau = 2$ (Fig. 13(b)). The color scheme is as follows. First iterate in black, second iterate in blue, third iterate in green, fourth iterate in red. The curves relative to the second iterate are not visible as they overlap with the ones relative to the fourth iterate.

viscosity produces in general a reduction of the stability range for the various iterates of the proposed predictor/multi-corrector algorithm. This fact can more clearly observed by comparing Figure 3 with Figure 12 and Figure 4 with Figure 13. It is also important to observe in Figure 13(b) that, in the case of two and four iterates for a stabilization parameter $c_\tau = 2$, the highest wave numbers *are not responsible* for the stability constraint, since, as the Courant number σ is increased, it is the mode at approximately $\beta_k = 7/8$ to go unstable first. Instead, in the case $c_\tau = 1$, for which both the lagged and conservative version of the time integrator coincide, it is the highest wave number to be responsible for the stability limit.

Recalling that by definition and the developments in Section 5, $0 \le \sigma \le 1/\sqrt{c_\tau}$, and $0 \le \kappa \le 1/2$, a rearrangement of (59) yields the stability condition:

$$\sigma \le \sqrt{\frac{1-2\kappa}{c_\tau}}\,, \tag{83}$$

from which, when $\kappa = 1/4$, we obtain $\sigma \le \sqrt{2}/2$ and $\sigma \le 1/2$ for the cases $c_\tau = 1$ and $c_\tau = 2$, respectively. These results can also be verified in Figure 13, for $\beta_k = \pi$. The convergence of the spectral radii relative to the various iterates to the implicit case can be evaluated in Figure 14 where sections of the elevation plots of Figure 11 at various values of the parameter σ are presented.

Perhaps the most important plots of the entire study are presented in Figure 15, in which red three-dimensional contour surfaces show the loci of the spectral radii equal to unity for the first, second, and third iterate of the proposed method, in the space $[\sigma, \beta_k, \kappa]$. Results are shown in the case of no stabilization ($c_\tau = 0$) and for values of the stabilization parameter $c_\tau = 1$ and $c_\tau = 2$, for the conservative approach. A blue surface represents the stability limit given by the high wave number analysis result (59) when equality holds. In addition, in Figure 15(f), a green surface is used to represent the condition,

$$1 = \frac{0.9}{\kappa + \sqrt{\kappa + c_\tau \sigma^2}}\,, \tag{84}$$

which incorporates a safety factor $CFL = 0.9$ in the time-step stability condition (61). First of all, note that the three-dimensional stability region in Figures 15(a) and 15(g) is bounded by the two red surfaces. The third iterate with no stabilization is unconditionally unstable, since the intersection between planes [κ = const.] and red surfaces always occurs in Figure 15(g). This is not the case for the first iterate, which is conditionally stable in the range $\kappa \in [1/4, 1/2]$. However, this result does not have practical relevance, since in the nonlinear case one can expect κ to cover the entire range $[0, 1/2]$.

Considering Figure 15(f) for the two-iterate scheme with $c_\tau = 2$, it is easy to realize that the red and blue surfaces do intersect at values $\beta_k < \pi$, indicating that the stability condition (61) is inappropriate. Mitigating the size of the time step by a factor 0.9 (see (84)) is sufficient in preventing the predictor-corrector to become unstable, as indicated by the fact that (at least by visual inspection) the red and green surfaces in the same picture do not intersect.

When $c_\tau = 1$, the estimate given by (61) (or, equivalently, (59)), yields a stable time step, at least by inspection of Figures 15(b), 15(e), and 15(h). The value $c_\tau = 2$ was used in the computations performed in [12], in combination with the following time-step control:

$$\Delta t = CFL\,\frac{h^2}{\nu + \sqrt{\nu^2 + c_\tau c_s^2 h^2}}\,, \quad \text{with} \quad CFL \le 0.9\,. \tag{85}$$

8. Numerical tests

We present two one-dimensional tests to show how the time step estimate derived in Section 5 performs in the general nonlinear case. In particular, the tests are performed for an ideal

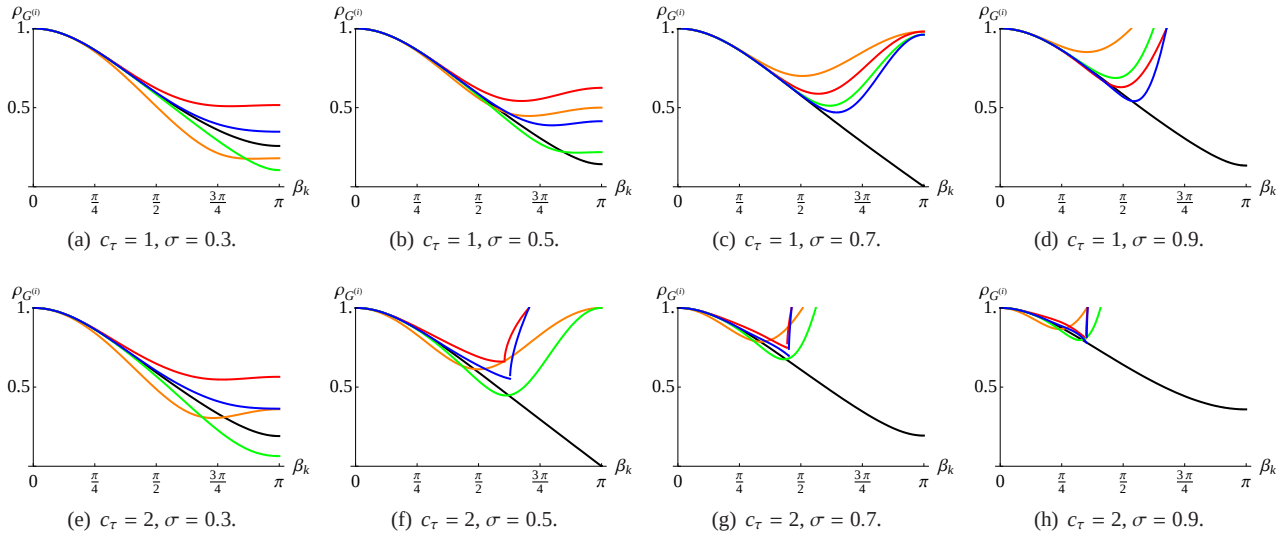

(a) $c_\tau = 1, \sigma = 0.3$. (b) $c_\tau = 1, \sigma = 0.5$. (c) $c_\tau = 1, \sigma = 0.7$. (d) $c_\tau = 1, \sigma = 0.9$.

(e) $c_\tau = 2, \sigma = 0.3$. (f) $c_\tau = 2, \sigma = 0.5$. (g) $c_\tau = 2, \sigma = 0.7$. (h) $c_\tau = 2, \sigma = 0.9$.

Figure 14: Spectral radii for the stabilized predictor/multi-corrector algorithm in the case $\kappa = 1/4$, for various values of the acoustic Courant number σ and stabilization parameter c_τ. Figures 14(a)–14(d), conservative scheme with $c_\tau = 1$, Figures 14(e)–14(h) conservative scheme for $c_\tau = 2$. Color scheme is as follows. Black: Implicit time integrator. Orange, red, green and blue are used for the first, second, third, and fourth iterate, respectively.

gas, using the nonlinear algorithm detailed in [12], from which the linearized version analyzed in this study has been derived.

8.1. Propagation of an acoustic pulse

This test tracks the propagation of an acoustic pulse represented by the initial conditions

$$v_0 = \omega \,, \tag{86}$$

$$\rho_0 = 1 + \omega \,, \tag{87}$$

$$p_0 = 1 + \omega \,, \tag{88}$$

$$\omega(X) = \begin{cases} \dfrac{1-\cos\left(\frac{2\pi\left(X-X_{off}\right)}{\lambda}\right)}{100} \,, & 0 \le X - X_{off} \le \lambda \,, \\ 0 \,, & \text{otherwise} \,, \end{cases} \tag{89}$$

where λ, the wavelength is taken equal to one fourth of the length the domain Ω_0, and $X_{off} = -\lambda$. The initial condition is depicted in Figures 16, 17, and 18, by red continuous lines. This test was already presented in [9–11] in full detail. In practice, the initial condition is given by a base flow with a superposed perturbation with amplitude of about 2%. We can therefore expect the nonlinear equations of Lagrangian shock hydrodynamics to behave very similarly to their linearized limit, discussed in full detail in the previous sections. As time progresses three waves are generated:

1. A large amplitude acoustic wave moving from left to right, which can be seen on the right of the domain.
2. A smaller amplitude acoustic wave moving from right to left, which at the final time of the computation is about to reflect from the left boundary.
3. A standing (i.e., motionless) entropy wave, characterized by a fluctuation in density and internal energy, visible on the left of the domain.

The numerical results are presented in Figures 16, 17, and 18, in the case of two, three, and four iterations of the predictor/multi-corrector algorithm, and for values of the CFL number equal to 0.90, 1, and 1.05. In the tests under consideration, the artificial viscosity operator is deactivated, and we adopt a constant $c_\tau = 2$. It is easy to realize that in the case of two and three iterations (Figs. 16 and 17, resp.) the time-step estimate is very sharp. In fact, in the two-iteration case of Figure 16, solutions are stable for $CFL = 0.9$ and unstable for $CFL = 1.0$. In the three-iteration case of Figure 17, solutions are stable up to $CFL = 1.0$, and become unstable for $CFL = 1.05$. The case of four iteratios (Fig. 18) is more interesting, since it shares the same theoretical stability bound as the two iterate case, namely $CFL = 0.9$, but oscillations appear only for $CFL = 1.05$. A possible explanation is that the nonlinear algorithm conserves total energy, and is therefore less prone to a catastrophic growth of instabilities, as the predictor/multi-corrector converges to the implicit limit.

8.2. Periodic Breaking Wave

Another interesting numerical test is represented by a periodic, nonlinear breaking wave problem similar to the one described in [2, 3]. The domain of the problem is the interval $[0, 1]$, subdivided into 100 elements, and with periodic boundary conditions. The material is a gamma-law ideal gas [6] with $\gamma = 5/3$. The initial density has a sinusoidal variation

$$\rho(x, 0) = 0.001\,(1.0 + 0.1\sin(2\pi x)) \,.$$

The initial pressure is

$$p(x, 0) = 10^6\left(\frac{\rho(x, 0)}{0.001}\right)^\gamma \,,$$

and the initial velocity is

$$v(x, 0) = 2\frac{c_{s_0} - c_s}{\gamma - 1} \,,$$

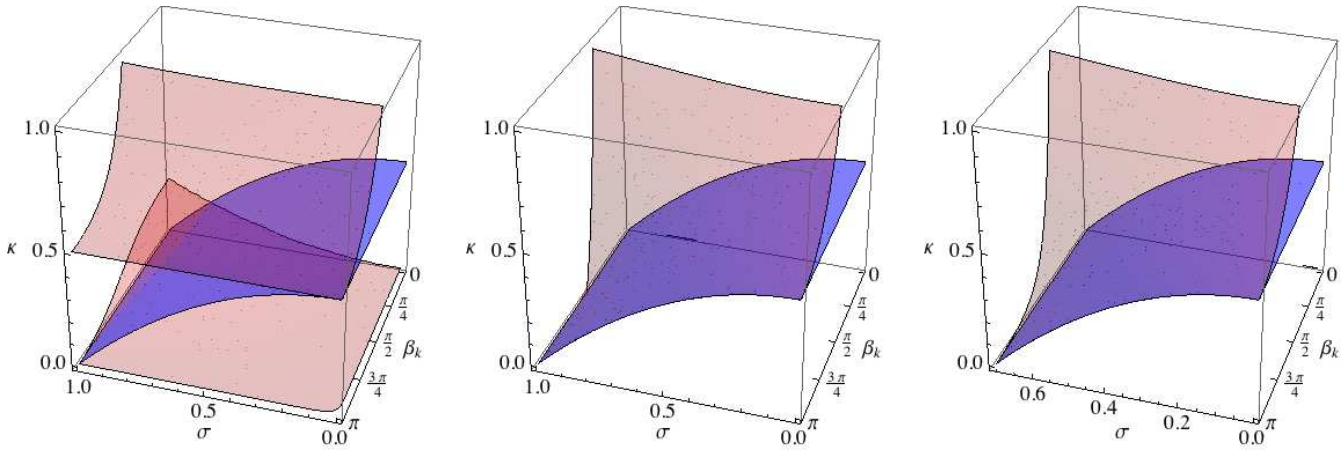

(a) $c_\tau = 0$, 1st iterate. (b) $c_\tau = 1$, 1st iterate. (c) $c_\tau = 2$, 1st iterate.

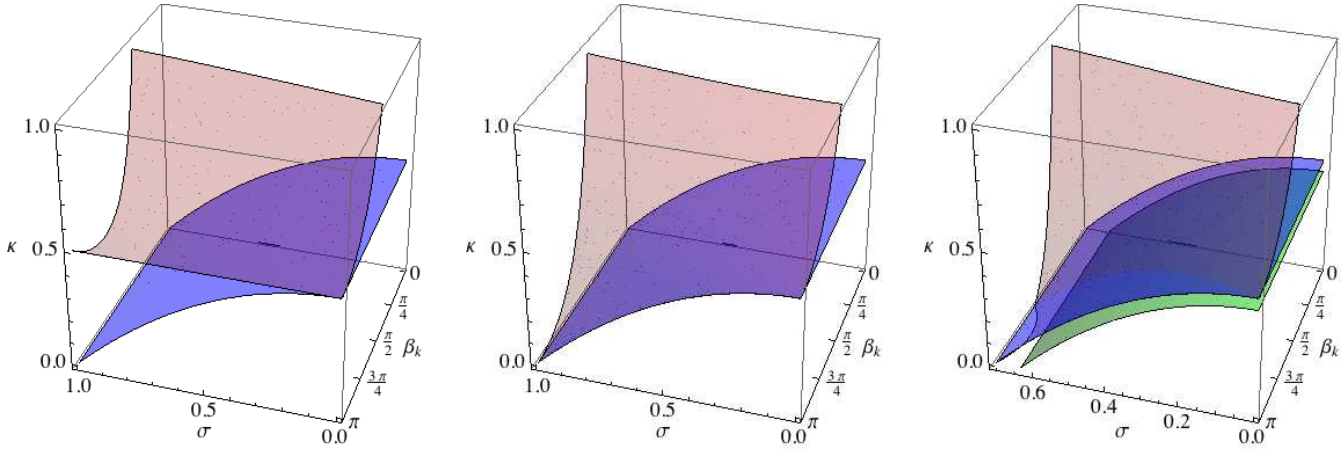

(d) $c_\tau = 0$, 2nd iterate. (e) $c_\tau = 1$, 2nd iterate. (f) $c_\tau = 2$, 2nd iterate.

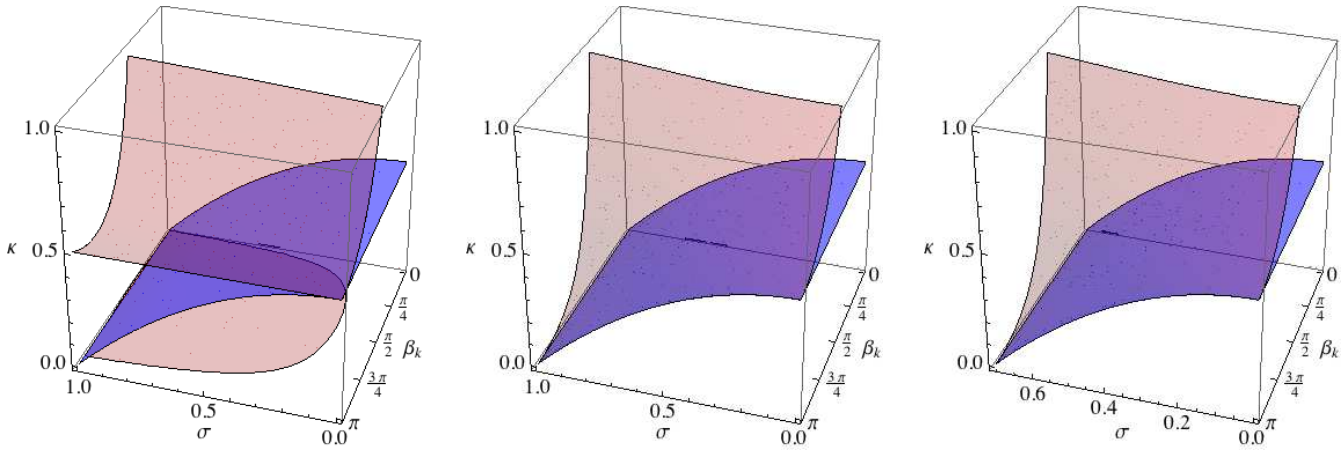

(g) $c_\tau = 0$, 3rd iterate. (h) $c_\tau = 1$, 3rd iterate. (i) $c_\tau = 2$, 3rd iterate.

Figure 15: Three-dimensional surfaces representing the loci of the spectral radii equal to unity for the first, second, and third iterate of the conservative version of the proposed time integrator, in the case of no stabilization, $c_\tau = 0$, and for values of the stabilization parameter equal to $c_\tau = 1$ and $c_\tau = 2$, respectively. The blue surface represents the stability limit given by (59) (or, equivalently, (61)), the green surface represents the "mitigated" stability condition given in (84). Note that there are no additional intersections between the red and blue surface in Figure 15(b), other than the one that occurs for $\beta_k = \pi$. The very rapid change in slope near $[\sigma, \beta_k] = [1, \pi/2]$ seems to create a graphical artifact, which was not possible to resolve increasing the plotting mesh resolution.

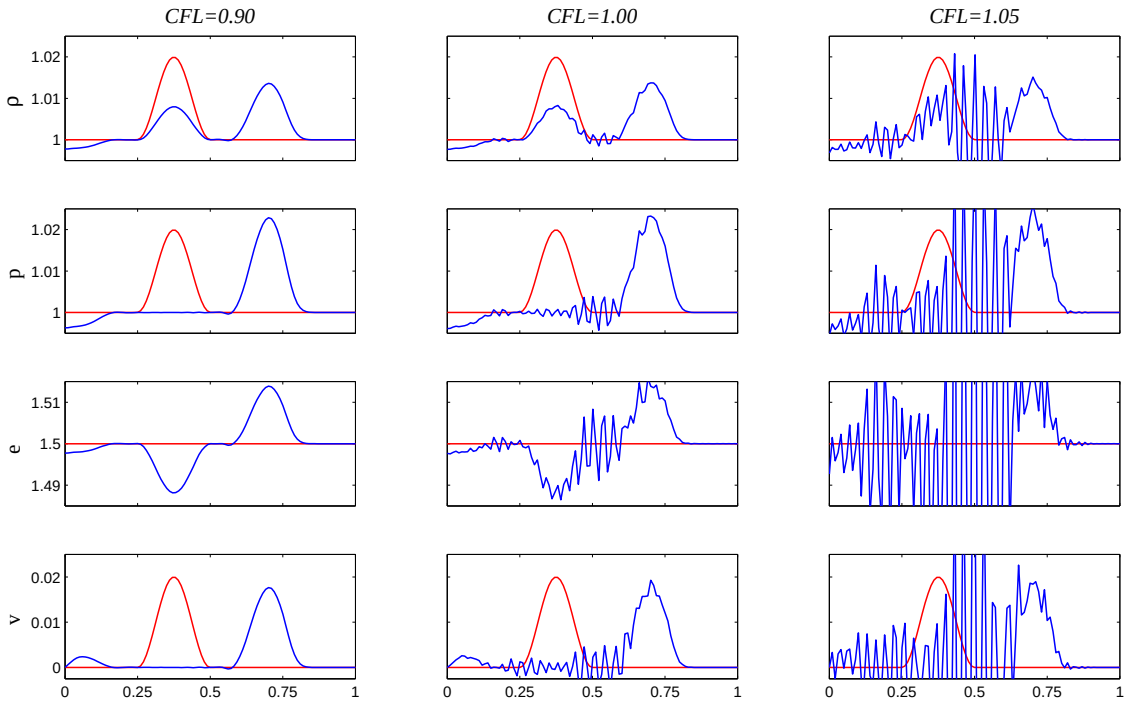

Figure 16: Plots of density, pressure, internal energy, and velocity versus the spatial position for the propagation of an acoustic pulse at time $t = 0.5$, and various CFL numbers. Two iterations of the conservative predictor/multi-corrector approach. The red lines indicate the initial condition.

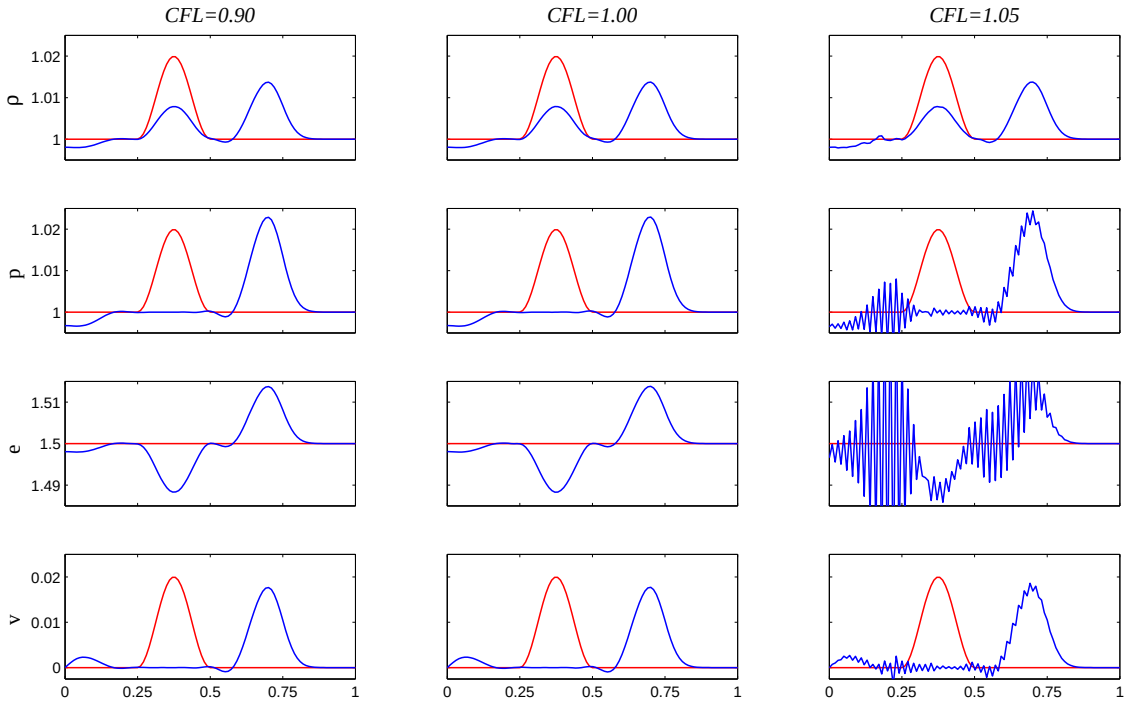

Figure 17: Plots of density, pressure, internal energy, and velocity versus the spatial position for the propagation of an acoustic pulse at time $t = 0.5$, and various CFL numbers. Three iterations of the conservative predictor/multi-corrector approach. The red lines indicate the initial condition.

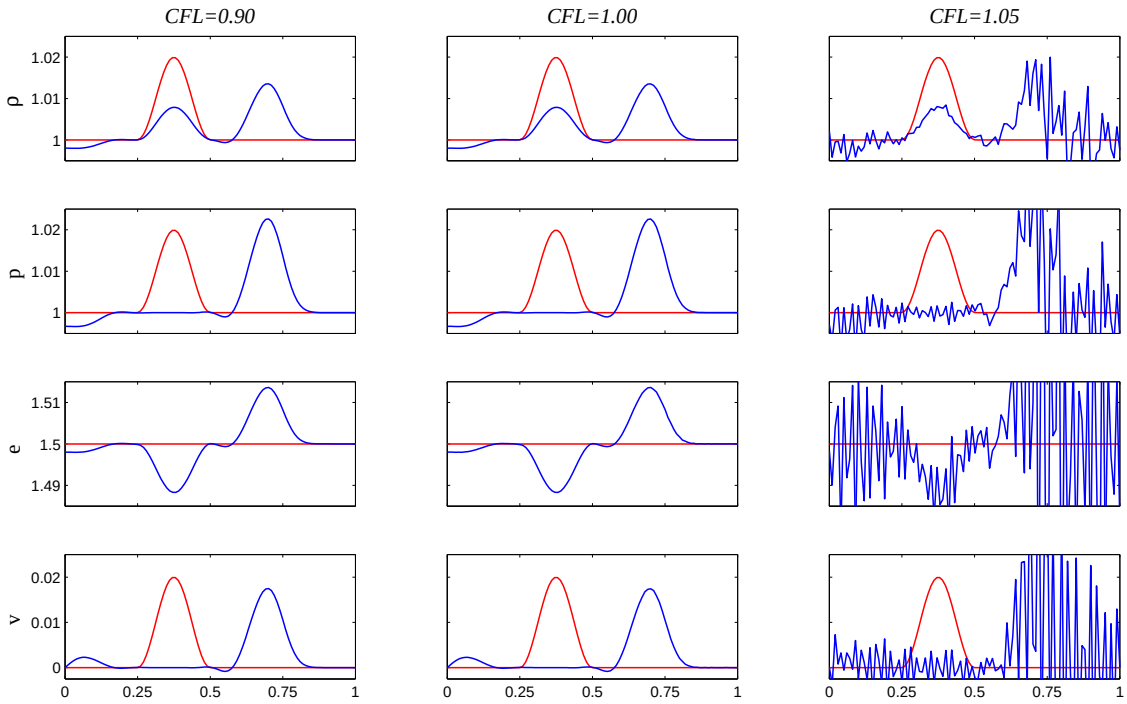

Figure 18: Plots of density, pressure, internal energy, and velocity versus the spatial position for the propagation of an acoustic pulse at time $t = 0.5$, and various CFL numbers. Four iterations of the conservative predictor/multi-corrector approach. The red lines indicate the initial condition.

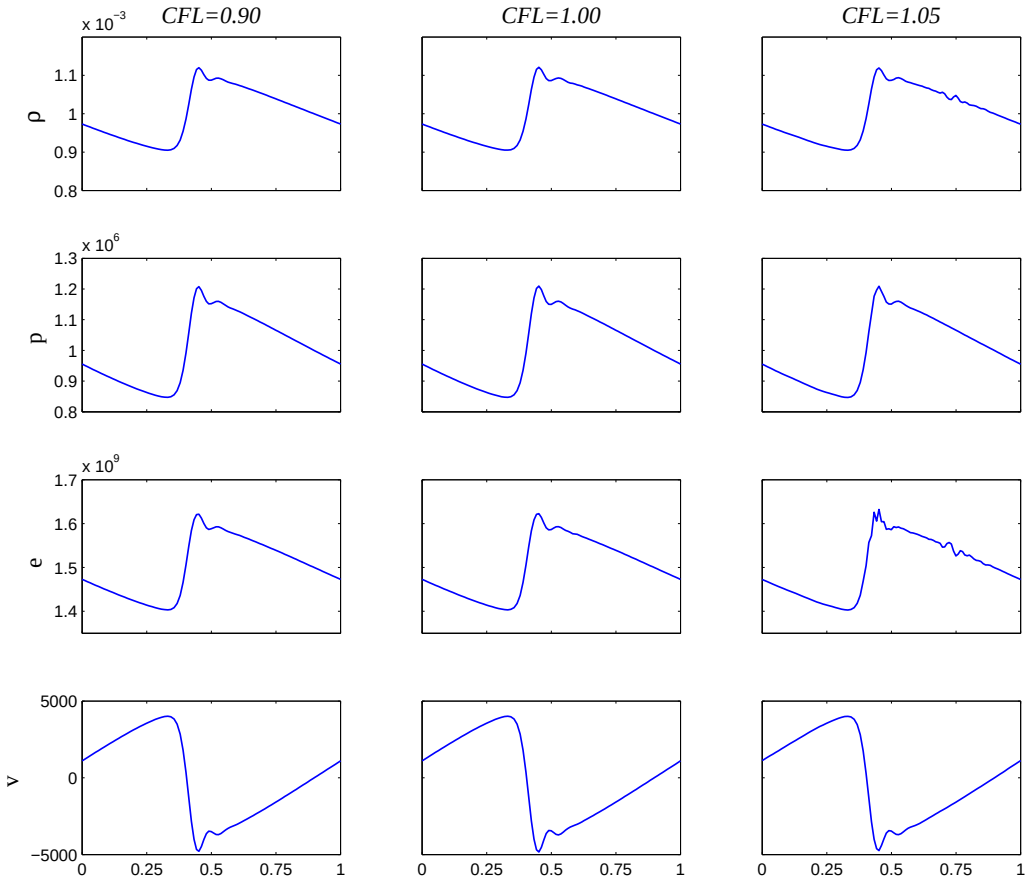

Figure 19: Plots of density, pressure, internal energy, and velocity versus the spatial position for the periodic breaking wave test at time $t = 0.0004$, and various CFL numbers. Three iterations of the conservative predictor/multi-corrector approach.

where

$$c_s = \left(\gamma \frac{p(x,0)}{\rho(x,0)}\right)^{1/2},$$

and

$$c_{s_0} = \left(\gamma \frac{10^6}{0.001}\right)^{1/2}.$$

The solution is smooth for a finite time $0 < T_{\text{break}} < \infty$, at which point the wave breaks and a shock forms [2, 3]. In this second test the artificial viscosity operator is active, with constants given as in [12]. The numerical results are presented for $t = 0.0004 > T_{\text{break}}$.

Because this problem involves the formation of shock waves, the applicability of the linearized analysis developed in previous sections is tested more severely. In particular, in the case of nonlinear problems, the predictor/multi-corrector approach is equivalent to a fixed-point *nonlinear* iteration. It was observed that two iterations were not sufficient to ensure nonlinear convergence of the solution for this test. Hence, only results for three and four iterations are presented, in Figures 19 and **??**, respectively.

Remark9. A reason for the need of at least three iterations may be the interplay between the artificial viscosity and the variational multiscale stabilization at the shock location. In particular, the artificial viscosity produces an "artificial" residual near the shock, which in turn increases the strength of the stabilization term. This nonlinear interaction may require more than two iterations to be captured with sufficient accuracy.

In the case of three and four iterations (Fig. 19 and Fig. **??**, resp.), oscillations are only visible for $CFL = 1.05$, proving the effectiveness of the time-step estimate in the nonlinear case. It is also noticeable that the overshoot past the shock is reduced in the four iterations case, with respect to the three iteration case. In the case of four iterates, instabilities should occur past $CFL = 0.90$, but they are not visible in the case $CFL = 1.00$, as in the acoustic pulse test.

Remark10. In the case of the periodic breaking wave test, the artificial viscosity is active and may provide a stabilizing effect by damping small oscillations in the compression region, which eventually coalesces into a shock. This fact may partially explain the results in the case of four iterates of the predictor/multi-corrector.

Remark11. In any case, the important point to be made is that the theoretical stability bound developed with a linearized analysis provides a safe estimate for time-step advancement also in the nonlinear case, as confirmed in the numerical computations presented in this study and in [12].

9. Summary

We have presented a von Neumann analysis of a linearized version of the predictor/multi-corrector algorithm proposed in [12], with a comprehensive evaluation of stability and dispersion properties. We have derived a time-step stability bound in the linear case that worked well also in the nonlinear case [12]. From the derivation presented herein, it appears that running the computations with a CFL safety factor of 0.8 yields better, if not the best results in terms of high wave number dissipation and dispersion error. Finally, formal order of accuracy arguments suggest that the proposed method is second order in space and time for smooth solutions, when (as usual in transient dynamics computations) time step and mesh spacing are balanced by a CFL-type condition. In conclusion, this article supports with a detailed analysis the algorithmic design of the method developed in [8] and implemented in [12], and shows that the effect of variational multiscale operators in shock hydrodynamics computations is to improve the stability and dispersion characteristics of time integrators without adding overly restrictive conditions on the time step.

Acknowledgments

The authors would like to thank Professor T. J. R. Hughes, at the University of Texas in Austin, for very valuable discussions. The authors would also like to thank Dr. R. Summers and Dr. S. Collis, for support and encouragement during the early stages of development of this research work.

References

[1] M. L. Abell and J. P. Braselton. *Mathematica by Example*. Academic Press, 4th edition, 2008.

[2] A. W. Cook and W. H. Cabot. A high-wavenumber viscosity for high-resolution numerical methods. Technical Report UCRL-ID-152002, Lawrence Livermore National Laboratory, Livermore, CA, 2003.

[3] A. W. Cook and W. H. Cabot. A high-wavenumber viscosity for high-resolution numerical methods. *Journal of Computational Physics*, **195**(2):594–601, 2004.

[4] A. Curnier. *Computational Methods in Solid Mechanics*. Kluwer Academic Press, Amsterdam, 1994.

[5] R. A. Horn and C. R. Johnson. *Matrix Analysis*. Cambridge University Press, Cambridge, UK, 1985.

[6] R. Menikoff and B. J. Plohr. The Riemann problem for fluid flow of real materials. *Reviews of Modern Physics*, **61**(1):75–130, 1989.

[7] A. R. Mitchell and D. F. Griffiths. *The Finite Difference Method in Partial Differential Equation*. John Wiley, London, 1980.

[8] G. Scovazzi. Stabilized shock hydrodynamics: III. A new stabilization concept for Lagrangian Computations. Computer Methods in Applied Mechanics and Engineering, 2009. Submitted.

[9] G. Scovazzi, M. A. Christon, T. J. R. Hughes, and J. N. Shadid. Stabilized shock hydrodynamics: I. A Lagrangian method. *Computer Methods in Applied Mechanics and Engineering*, **196**(4–6):923–966, 2007.

[10] G. Scovazzi, E. Love, and M. J. Shashkov. A multi-scale Q1/P0 approach to Lagrangian shock hydrodynamics. Technical report, SAND2007-1423, Sandia National Laboratories, New Mexico, March 2007. Available at: `http://www.cs.sandia.gov/~gscovaz`.

[11] G. Scovazzi, E. Love, and M. J. Shashkov. A multi-scale Q1/P0 approach to Lagrangian shock hydrodynamics. *Computer Methods in Applied Mechanics and Engineering*, **197**(9–12):1056–1079, 2008.

[12] G. Scovazzi, J. N. Shadid, E. Love, and T. J. R. Hughes. Stabilized shock hydrodynamics: IV. Computations with a conservative updated Lagrangian method. Computer Methods in Applied Mechanics and Engineering, 2009. Submitted.

[13] L. I. Sedov. *Similarity and Dimensional Methods in Mechanics*. Academic Press, New York, 1959.

[14] J. C. Strikwerda. *Finite Difference Schemes and Partial Differential Equations*. Chapman & Hall, New York, 1989.

[15] S. Wolfram. *The Mathematica Book*. Cambridge University Press, 4th edition, 1999.

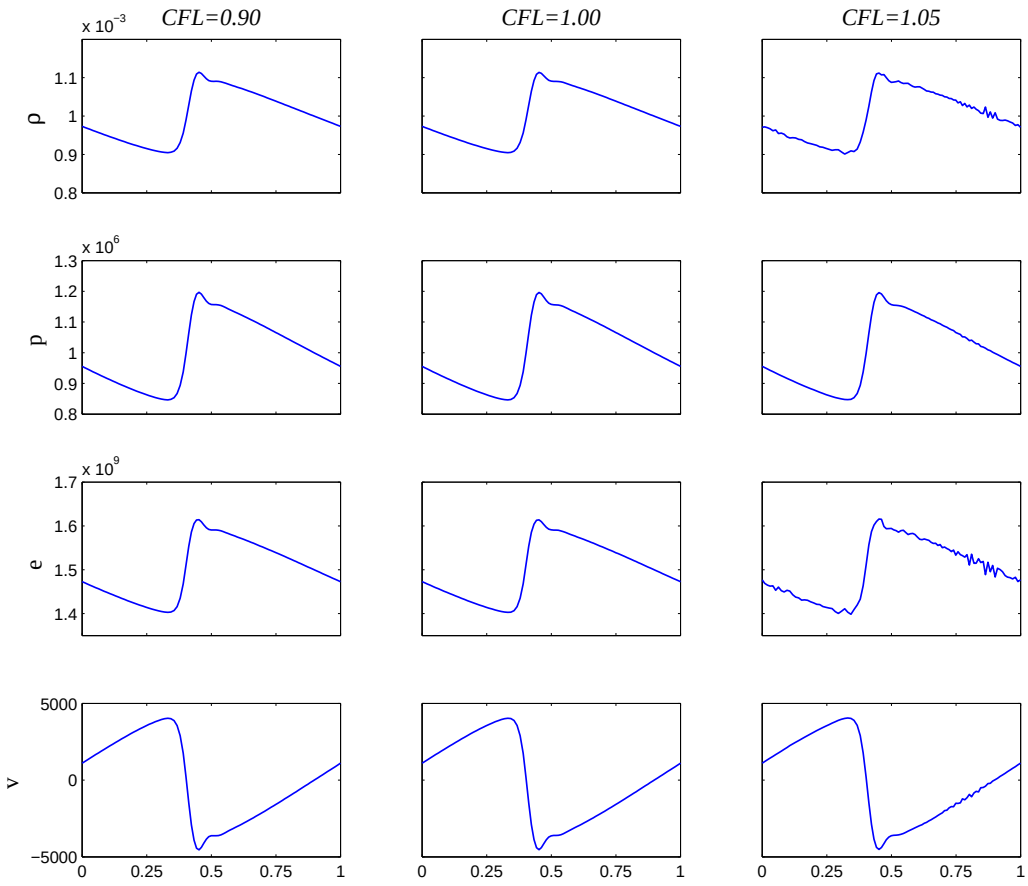

Figure 20: Plots of density, pressure, internal energy, and velocity versus the spatial position for the periodic breaking wave test at time $t = 0.0004$, and various CFL numbers. Four iterations of the conservative predictor/multi-corrector approach.